





**SVEN LANGE**

Spectroscopic and phase-stabilisation  
properties of pure and  
rare-earth ions activated  $\text{ZrO}_2$  and  $\text{HfO}_2$



TARTU UNIVERSITY  
**PRESS**

The study was carried out at the Institute of Physics, University of Tartu.

The Dissertation was admitted on April 23, 2010 in partial fulfilment of the requirements of the degree of doctor of Philosophy (solid state physics), and allowed for defence by the Council of the Institute of Physics, University of Tartu.

Supervisors:	Dr. Ilmo Sildos Institute of Physics, University of Tartu, Estonia Prof. Mikhail Brik Institute of Physics, University of Tartu, Estonia
Opponents	Dr.habil.phys. Donats Millers Division of Disordered Material Physics, Institute of Solid State Physics, University of Latvia, Riga, Latvia Prof. Jüri Krustok Department of Material Science, Faculty of Chemical and Materials Technology, Tallinn University of Technology, Estonia
Commencement	June 17, 2010 at the University of Tartu, Tartu, Estonia

The publication of the thesis is supported by TÜ and TTÜ doctoral school “Funktsionaalsed materjalid ja tehnoloogiad” (FMTDK) ESF project no. 2.2.0401.09-0079.



ISSN 1406–0647  
ISBN 978–9949–19–370–7 (trükis)  
ISBN 978–9949–19–371–4 (PDF)

Autoriõigus Sven Lange, 2010

Tartu Ülikooli Kirjastus  
[www.tyk.ee](http://www.tyk.ee)  
Tellimuse nr 248

# CONTENTS

LIST OF ORIGINAL PAPERS .....	7
AUTHOR'S CONTRIBUTION .....	8
LIST OF USED APPREVIATIONS .....	9
1. INTRODUCTION.....	10
1.1. Aim of the work.....	11
2. TRANSITION METAL OXIDES ZRO <sub>2</sub> AND HFO <sub>2</sub> .....	12
2.1. Introduction .....	12
2.2. Intrinsic and defect related luminescence in ZrO <sub>2</sub> and HfO <sub>2</sub> .....	13
2.3. Rare earth ions as optically active dopants.....	13
2.4. RE luminescence excitation and relaxation processes.....	15
2.5. Rare-earth ions as phase stabilisators .....	19
3. SAMPLE PREPARATION.....	21
3.1. Introduction .....	21
3.2. ALD process .....	21
3.3. Sol-gel process.....	22
3.4. Skull melting process.....	24
3.5. Ion implantation.....	25
3.6. Overview of prepared zirconia and hafnia samples.....	27
4. SPECTROSCOPIC INVESTIGATION OF RE <sup>3+</sup> DOPED ZRO <sub>2</sub> AND HFO <sub>2</sub> [PAPERS I–V] .....	29
4.1. Introduction .....	29
4.2. Experimental setup .....	30
4.3. Undoped sol-gel and ALD prepared films [papers I,II,IV] .....	31
4.4. Ion implanted ALD films [paper I].....	34
4.5. Sol-gel prepared HfO <sub>2</sub> [paper II].....	36
4.6. Solidification of melt prepared ZrO <sub>2</sub> [paper III] .....	39
4.7. Decay analysis .....	40
4.8. Further discussion.....	42
5. SM <sup>3+</sup> AS CRYSTALLOGRAPHIC PROBE IN ZRO <sub>2</sub> [PAPERS III–IV] .....	44
5.1. Introduction .....	44
5.2. Experimental setup .....	44
5.3. Results .....	45
5.3.1. Raman measurements .....	45
5.3.2. CEES measurements.....	47
5.3.3. PL decay measurements .....	49

5.3.4. Excitation mechanisms .....	50
5.3.5. Spatial mapping .....	51
5.3.6. Proposed model for phase segregation .....	52
 6. PHASE STABILIZATION OF SOL-GEL MICROROLLS	
[PAPER V] .....	54
6.1. Introduction .....	54
6.2. Experimental setup .....	54
6.3. Results and discussion .....	55
6.4. Conclusion .....	58
 SUMMARY .....	59
SUMMARY IN ESTONIAN .....	60
 REFERENCES .....	61
 ACKNOWLEDGEMENTS .....	65
 PUBLICATIONS .....	67
 CURRICULUM VITAE (CV) .....	111
ELULOO KIRJELDUS (CV) .....	113

## LIST OF ORIGINAL PAPERS

- I. S. Lange, V. Kiisk, V. Reedo, M. Kirm, J. Aarik and I. Sildos, “*Luminescence of RE-ions in HfO<sub>2</sub> thin films and some possible applications.*”, Optical Materials 28 (2006), 1238–1242
- II. S. Lange, V. Kiisk, J. Aarik, M. Kirm and I. Sildos, “*Luminescence of ZrO<sub>2</sub> and HfO<sub>2</sub> thin films implanted with Eu and Er ions*”, Physica Status Solidi (c) 3 (2007), 938–941
- III. S. Lange, I. Sildos, M. Hartmanova, J. Aarik and V. Kiisk, “*Luminescence properties of Sm<sup>3+</sup>-doped polycrystalline ZrO<sub>2</sub>*”, Journal of Non-Crystalline Solids 354 (2008), 4380–4382
- IV. V. Kiisk, S. Lange, K. Utt, T. Tätte, H. Mändar and I. Sildos, “*Photoluminescence of sol-gel-prepared hafnia*”, Physica B: Condensed Matter 405 (2) (2010), 758–762
- V. S. Lange, I. Sildos, M. Hartmanova, V. Kiisk, E. E. Lomonova and M. Kirm, “*Optical Investigation of Sm doped ZrO<sub>2</sub>*”, Journal of Physics: Conference Series (2010), Accepted for publication
- VI. K. Utt, S. Lange, M. Järvekülg, H. Mändar, P. Kanarjov, I. Sildos, “*Structure and optical properties of Sm-doped ZrO<sub>2</sub> microrolls*”, Optical Materials (2010), In Press

Earlier papers related to current work

- VII. Sildos, V. Kiisk, S. Lange and J. Aarik, “*Time-resolved exciton-emission spectroscopy of anatase*”, Proceedings of SPIE 5122 (2003), 56–59
- VIII. S. Lange, I. Sildos, V. Kiisk and J. Aarik, “*Energy transfer in the photo-excitation of Sm<sup>3+</sup> implanted TiO<sub>2</sub> thin films*”, Materials Science and Engineering B 112 (2004), 87–90
- IX. I. Sildos, S. Lange, T. Tätte, V. Kiisk, M. Kirm and J. Aarik, “*Emission of rare earth ions incorporated into metal oxide thin films and fibres*”, Mat. Res. Soc. Symp. Proc. 796 (2004), 361–366
- X. V. Reedo, S. Lange, V. Kiisk, A. Lukner, T. Tätte and I. Sildos, “*Influence of ambient gas on the photoluminescence of sol-gel derived TiO<sub>2</sub>:Sm<sup>3+</sup> films*”, Optical Materials and Applications, Proceedings of SPIE 5946 (2005), 59460F1-6
- XI. V. Kiisk, I. Sildos, S. Lange, V. Reedo, T. Tätte, M. Kirm and J. Aarik, “*Photoluminescence characterization of pure and Sm<sup>3+</sup>-doped thin metaloxide films*”, Applied Surface Science 247 (2005), 412–417
- XII. S. Lange, I. Sildos, V. Kiisk, M. Kirm, “*Photoluminescence of RE-doped thin metal-oxide films*”, Physica Status Solidi (c) 2 (1) (2005), 326–329
- XIII. J. Aarik, A. Kasikov, M. Kirm, S. Lange, T. Uustare and H. Mändar, “*Optical properties of crystalline Al<sub>2</sub>O<sub>3</sub> thin films grown by atomic layer deposition*”, Proc. of SPIE 5946 (2005), 594601

## **AUTHOR'S CONTRIBUTION**

Author's own contribution to the work described here and presented in the accompanying papers has been substantial. Without emphasising any paper in particular the author has in all cases been the main contributor to spectroscopic measurements execution as well as data presentation. Author's contribution to theoretical discussions and paper writing has been an ongoing effort with measurable contribution to papers I–IV. In papers V and VI the author's work is considered as the ideological base for the delivered message.

It must be noted that sample preparation has not been within the capabilities of the author (with exception being ion-implantation and annealing). Therefore investigated samples are in all cases at least partly been provided by other groups specialised in the different preparation techniques described.



## LIST OF USED APPREVIATIONS

ALD	Atomic layer deposition
AMOLED	Amorphous organic light emitting diode
CB	Conduction band
CCD	Charge coupled device
CEES	Combined excitation-emission spectroscopy
CTB	Charge transfer band
CVD	Chemical vapour deposition
DOS	Density of states
eV	Electron volt
FRET	Fluorescence resonant energy transfer
FWHM	Full with half maximum
HREED	Reflection high energy electron diffraction
ICCD	Intensified charge coupled device
IUPAC	International Union of Pure and Applied Chemistry
LED	Light emitting diode
OPO	Optical parametric oscillator
PL	Photoluminescence
QCM	Quartz crystal microbalance
RE	Rare earth
RF	Radio frequency
RT	Room temperature
SEM	Scanning electron microscope
TRIM	Transport of ions in matter
UV	Ultraviolet
VUV	Visible ultraviolet
XRD	X-Ray diffraction

## I. INTRODUCTION

Wide band-gap oxides, both pure and doped with different impurities, are extensively studied systems because of their numerous applications in many optical, mechanical and electronic devices and solutions. Because of relatively large transparency window, engineering and investigation of visible and ultra-violet (UV) luminescence and its generation properties in the latter are widespread. They can be used to create luminophores with great variety covering the whole visible and visible ultraviolet (VUV) range. They can be found in cathode ray tubes, luminescent lamps, LEDs and plasma displays. Other somewhat less common uses include X-ray imaging, dosimetry, night vision displays, persistent luminescent markers (phosphors), bio-markers, solar cells and AMOLED displays [1–7]. Characteristic decay times of the luminophores can vary greatly depending on the application from as low as 16 ns in  $\text{LaBr}_2\text{:Ce}^{3+}$  [1] (efficient X- and  $\gamma$ -ray scintillator) to two orders of magnitude slower 1.3 ms in plasma display phosphor  $\text{Y}_2\text{O}_3\text{:Eu}^{3+}$  [2]. At the other extreme persistent luminescence materials like  $\text{SrAl}_2\text{O}_4\text{:Eu}^{2+},\text{Dy}^{3+}$  can reveal afterglow for more than 10 hours [3].

Another field where wide band-gap oxides are becoming increasingly important is semiconductor industry. As the era of silicon based electronics nears its end due to unavoidable leakage currents at nanoscale new high-k materials are continuously being searched for replacement. So far the biggest achievement in the field has been the incorporation of amorphous hafnium oxide into the 45 and 32 nm production processes. The shrinking of gate dimensions is expected to continue to 22 nm to finally 5 nm in 2020–2030 [5]. At such scales the exact control of material's phase stabilization becomes increasingly important as defects related to crystal imperfections could cause leakage currents or even failures. For investigation of the morphology of such small quantities of matter, new methods of crystal phase detection must be developed. Compared to conventional X-ray diffraction (XRD) and Raman scattering methods, effective characterisation of the latter needs higher spatial accuracy and lower detection thresholds.

Although these systems are studied by many research groups and the number of publications devoted to their physical properties is growing, many questions remain unsolved or there exists a certain controversy in interpretation of experimental results. In particular, the role of defects in formation of optical spectra is not fully understood yet, especially, the energy of these defects' formation, their distribution etc. Mechanisms of excitation of impurity ions via energy transfer through the intentionally created defects, are also not completely clear.

## **I.1. Aim of the work**

For partly addressing the problems raised in the last paragraph the present thesis will focus on investigating the photoluminescence and phase stabilization properties of rare-earth (RE) doped zirconium and hafnium oxides. The original contribution of the work is divided into two main parts. In the first part RE doped  $\text{ZrO}_2$  and  $\text{HfO}_2$  as luminescence materials are investigated with the aim to clarify the following points: the mechanisms of energy transfer from oxide host to RE ions, the influence of RE doping to the defect structure and luminescence efficiency and positions of the RE ions' energy levels within the oxide band-gap. The special experimental aim is to give as wide as possible coverage of differently prepared and impurity doped  $\text{ZrO}_2$  and  $\text{HfO}_2$  samples in order to account for as many as possible factors that could influence the PL properties.

The second part of the work covers extensive investigation of two different  $\text{Sm}^{3+}$  doped  $\text{ZrO}_2$  systems: solidification of melt prepared bulk samples and sol-gel prepared micro-rolls. The aim is to introduce and use a novel method for detecting phase composition and its spatial segregation in  $\text{ZrO}_2$  by using  $\text{Sm}^{3+}$  ion photoluminescence as a crystallographic probe.

In order to give a reader a better overview of the underlying theory, material properties and investigation techniques the proceeding work will be divided into following chapters:

- In Chapter 2 background information will be given about the luminescence processes as well as phase stabilisation dynamics of pure and RE doped  $\text{ZrO}_2$  and  $\text{HfO}_2$ .
- Chapter 3 will focus on the techniques and actual preparation of different  $\text{ZrO}_2$  and  $\text{HfO}_2$  samples studied in the experimental part. The choice of growth and doping methods includes: sol-gel powder precipitation, sol-gel micro-rolling, sol-gel tip-coating, solidification of melt and atomic layer deposition (ALD) accompanied by in-situ and ion-implantation based dopant incorporation.
- In Chapter 4 the results of spectroscopic measurements will be discussed and compared to theoretical calculations as well as earlier data. As a result, a clearer picture of intrinsic as well as rare-earth dopant related excitation processes in  $\text{ZrO}_2$  and  $\text{HfO}_2$  will be obtained.
- In Chapters 5 and 6 a new method for probing  $\text{ZrO}_2$  crystal structure via  $\text{Sm}^{3+}$  impurity will be investigated. The method is shown to be applicable for both bulk and micro scale investigation of phase content in  $\text{ZrO}_2$ .

## 2. TRANSITION METAL OXIDES ZrO<sub>2</sub> AND HfO<sub>2</sub>

### 2.1. Introduction

Zirconium and hafnium oxides have rather similar properties which is why they are often considered as twin oxides. The latter is caused by the fact that zirconium and hafnium atoms and respective ions are very similar in size because of the lanthanide contraction. Latter causes the atom and ion radii to contract rather than expand as electrons are added to the electron shell. As a result the ionic radius of Zr<sup>4+</sup> is 79 pm while that of Hf<sup>4+</sup> is 78 pm despite the higher number of electrons [8]. For comparison in lanthanide series from Ce to Lu the ionic radius decreases from 102 to 86 pm [9].

In nature hafnium only occurs in zirconium ores as a trace element at concentrations of 1–4 % [10]. Because of the similar electron configuration ([Kr] 4d<sup>2</sup> 5s<sup>2</sup>, [Xe] 4f<sup>14</sup> 5d<sup>2</sup> 6s<sup>2</sup>) and almost identical atomic and ionic radii the chemical behaviour of the elements is very similar and therefore purification of either one from the mixed ores is a very difficult process. The most common tactics for purification are: solvent extraction [11], ion exchange [12] and distillation of fused salts [13].

ZrO<sub>2</sub> and HfO<sub>2</sub> both can exist in several crystal modifications. The only stable polymorph at ambient conditions is monoclinic, which is converted to tetragonal and finally cubic at higher temperatures. These transitions take place at 1150 K and 2370 K [14] in ZrO<sub>2</sub> and at 1830 K [15] and 2870 K [17] in HfO<sub>2</sub> respectively.

To stabilise tetragonal or cubic forms at ambient temperatures, several routes have been proposed. Stabilisation of pure cubic HfO<sub>2</sub> has been achieved via growing nanocrystallites smaller than 4–6 nm in size [15]. For stabilising tetragonal phase diameters of < 30 nm have been reported to be sufficient [16]. A more conventional method for stabilising both HfO<sub>2</sub> and ZrO<sub>2</sub> is via doping with yttrium [18] or other rare-earth elements.

Technologically phase stabilisation and electronic properties of ZrO<sub>2</sub> and HfO<sub>2</sub> are highly interesting. As the downscaling of metal-oxide-semiconductor field effect transistors and capacitor structures with SiO<sub>2</sub> dielectrics has become difficult, insulators with higher dielectric constants are needed for replacement in these devices. Among the possible candidates, HfO<sub>2</sub> (especially in amorphous form) is one of the most promising materials. Additionally HfO<sub>2</sub> and ZrO<sub>2</sub> possess high densities (up to 11.78 and 6.21 g/cm<sup>3</sup>, respectively [19]) and high effective atomic numbers, required for efficient absorption of X-rays in a thin layer rendering them promising candidates for X-ray imaging technologies.

## 2.2. Intrinsic and defect related luminescence in $\text{ZrO}_2$ and $\text{HfO}_2$

Optical properties of  $\text{ZrO}_2$  and  $\text{HfO}_2$  are closely related to their electronic structure. In both oxides the valence band top is formed by oxygen 2p orbitals, whereas the conduction band consists of the  $\text{Zr}^{4+}$  4d and  $\text{Hf}^{4+}$  5d orbitals respectively [19]. The formed band-gap is direct in nature. Theoretical calculations have shown that in pure (“ideal”)  $\text{ZrO}_2$  substantial rise in density of states (DOS) starts from  $\sim 5$  eV forming an initial almost continuous conduction band that extends to 10 eV [20]. Experimentally determined band-gap values for both oxides vary. For zirconia values of 5.2 eV [21], 5.35 eV [19] or 5.74 eV [22] have been reported. For hafnia the band-gap energy is higher. Example values of 5.4 eV [23], 5.45 eV [24], 5.85 eV [19] and 5.8 [25] have been reported. Many of the variations are usually attributed to defect related absorptions thus the exact determination of the band gap value requires high quality crystalline samples. Experimental determination of the DOS from absorption or PL excitation is more complicated as the width of the low energy band is wide enough to be interfered by two photon absorption processes in both oxides [paper XI].

The intrinsic emission band of the pure oxides usually consists of a broad Gaussian shaped self-trapped Frenkel type exciton (STE) band located at 4.2–4.35 eV in  $\text{ZrO}_2$  and at 4.2–4.4 eV in  $\text{HfO}_2$ , respectively [19,26,27]. The STE states can easily be quenched via thermal activation into radiation defect states. The latter is routinely regarded as the cause for almost total quenching of the STE emission at room temperature (RT) [28].

An additional emission band observed often in both oxides at lower energies (2.5 – 3.5 eV) [19,29,30] is considered extrinsically originating from different defects. Because of its higher ionization threshold the emission is observed also at elevated temperatures. Main defects in studied oxides are various colour centres formed by oxygen vacancies in various configurations with trapped electrons.

## 2.3. Rare earth ions as optically active dopants

As defined by IUPAC, rare earth elements or rare earth metals are a collection of seventeen chemical elements in the periodic table, namely scandium, yttrium, and the lanthanoids (previously lanthanides). The lanthanoid series comprises the fifteen elements with atomic numbers 57 through 71, from lanthanum to lutetium. Scandium and yttrium are considered rare earths since they tend to occur in the same ore deposits as the lanthanoids and exhibit similar chemical properties. Rare-earth elements are chemically very similar, and all exhibit intense narrow-band luminescence across much of the visible and near infra-red

portions of the spectrum. Spectroscopic properties of the rare-earth ions arise primarily from their  $4f^N$  shell energy states in their tri- or divalent state.

Energy levels of free rare-earth ions are derived starting from classical Russell-Sounders approximation. Electrons in a free atom reside inside a shell and are characterised by a particular value of  $n$ , the principal quantum number. Within each shell electron can reside on  $l=n-l$  sub shells. These sub shells are sometimes referred to as  $s, p, d, f$  etc. orbitals, depending on the value of the orbital quantum number  $l$  ( $l=0,1,2,3$  for the  $s, p, d, f$  orbitals). A quantum mechanics approach to determining the energy of electrons in an atom or ion is based on the results obtained by solving the Schrödinger wave equation for the hydrogen atom. The various solutions for the different energy states are characterised by the three quantum numbers,  $n$ ,  $l$  and  $m_l$ . A fourth quantum number, which is denoted as  $m_s$  and describes the electron spin states, is also added to the final set of quantum numbers, uniquely describing a particular state. For finding out energy levels of an  $N$  electron atom a proper coupling scheme must be selected to sum up the momentum of electrons. According to the Russell-Sounders or LS coupling scheme (which is used in case of lighter atoms from the first half of the periodic table), the Coulomb interaction between electrons is much stronger than the spin-orbit interaction between the spin and angular momenta of each electron. The ground states of electron are then characterised (in addition to  $n$  and  $l$ ) by quantum numbers  $L$  (total orbital momentum) and  $S$  (total spin momentum). In addition, the operator  $J=S+L$  is called the total angular momentum and describes the interaction between total orbital and spin momenta of a particular electron configuration. These energy states are conveniently denoted as LS terms and referred to by notation  $^{2S+1}L_J$ . LS terms are  $2J+1$  time degenerate in respect to magnetic quantum number  $M=-J, -J+1, \dots, J$ . The states with different values of  $J$  have different energy, which is referred to as the fine structure of the LS terms. As a rule, the energy separation between the states with different  $J$  is much smaller than between different LS terms.

In heavier atoms where spin-orbital interaction becomes important compared to electrostatic interactions, a  $j-j$  coupling approximation gives better results. In this case, the spin  $s$  and orbital momenta  $l$  of an individual electron are summed up to give a total angular momentum  $j$  of this electron:  $j=l+s$ . Then the momenta  $j$  of individual electrons are summed up to produce a total angular momentum of a particular state of many-electron configuration. In case of rare-earth ions the energy states are a mixture of both LS and  $j-j$  coupling schemes and are still referred to as LS terms, which can reveal mixing among same JM states but with different LS values.

In crystal field the LS terms split further into the so called Stark components in respect to the quantum number  $M$ . The lower the crystal field symmetry the lower is the ground term degeneracy. According to Kramer's theorem, the maximum number of states arising from a  $J$ -manifold of an electronic configuration with odd number of electrons, is  $(2J+1)/2$ ; each level remains at

least doubly degenerated. Such two-fold degeneracy can be removed, in principle, by applying external magnetic field. For electronic configurations with even number of equivalent electrons, the J-state degeneracy can be removed completely and the number of the states is  $2J+1$ . In general the separation of the split levels is in the order of a few hundred  $\text{cm}^{-1}$ . Based on this it is expected that the luminescence spectra of rare-earth ions can be used as probes for local crystal field symmetry at the impurity centre. In several works [33,34] the electric dipole transition  $^5D_0-^7F_2$  of  $\text{Eu}^{3+}$  has been used to probe the site symmetry changes of low symmetry sites, where the  $^5D_0-^7F_1$  magnetic dipole transition is rather insensitive to local environment. Alternatively the crystal field splitting of  $\text{Sm}^{3+}$  ion has been used to probe crystal phase composition of tetragonal and monoclinic  $\text{ZrO}_2$  [35].

$4f^N$  shell transitions as luminescence sources are generally used in many different applications. The  $^4F_{3/2}-^4I_{11/2}$  transition of  $\text{Nd}^{3+}$  ion at  $1.05\mu\text{m}$  is used in YAG laser crystals [31].  $\text{Er}^{3+}$  luminescence at  $1.5\mu\text{m}$ , emitted from the first excited J-manifold  $^4I_{13/2}$  to the ground state ( $^4F_{15/2}$ ) is important because of its optimal wavelength for the transmission window in fiber-optical amplifiers and communication lines.

Another class of important spectroscopic features emerge from rare-earth ions' higher 5d orbitals. The 5d states differ from 4f states by their remarkably stronger coupling to crystal lattice vibrations and less localised nature. Furthermore inter configurational transitions from  $4f^{N-1}5d$  states are parity allowed resulting in  $10^4$  times higher absorption gross section compared to 4f–4f transitions. Due to the latter and relatively high energy needed for the excitation, these transitions are becoming popular in UV lasers and scintillator applications [32].

## 2.4. RE luminescence excitation and relaxation processes

Excitation efficiency of a luminescence centre is typically described by its absorption gross-section ( $\sigma$ ). Typical values for parity forbidden 4f–4f transitions are in the range from  $10^{-18}$  to  $10^{-20}\text{ cm}^{-2}$  rendering them rather ineffective.  $4f^{N-1}5d$  transitions have higher excitation efficiency ( $\sigma \sim 10^{-12}\text{ cm}^{-2}$ ) but are located in the UV and VUV region restricting their use in many applications.

For more effective excitation of 4f–4f transitions host mediated excitation via energy transfer from host to rare-earth dopant is a widely exploited approach.

In semiconductor solids the majority of charge carriers are localised or delocalised electrons and holes. Charge carriers could be created by external photons, electron bombardment, or charge carrier injection (p-n junctions). Regardless of their creation mechanisms they tend to recombine relatively fast.

Free electron-hole pairs have average lifetime in the order of nanoseconds and localised electron-hole pairs (excitons) of microseconds. Within this timeframe the charge carriers must transfer their energy to dopant ions in order to effectively excite luminescence. For energy transfer several scenarios can happen.

The charge carriers may recombine radiatively and emit a secondary photon that gets absorbed by the dopant ion. In the case of 4f–4f transitions this process is inherently low in efficiency, but can happen at more favourable energy than the primary excitation.

When charge carriers recombine at the immediate vicinity to impurity ion, a non-radiative recombination can occur resulting in multipole type energy transfer to the rare-earth ion, which strongly depends on the involved ions' wave functions overlap. Efficiency of this process is governed by the mobility of the charge carriers and the concentration of impurity ions.

The third possibility is so called Auger type energy transfer, when a non-resonant energy transfer to impurity ion takes place via Coulomb interaction rather than wave function overlapping. Any excess energy is removed in this case via an additional phonon or photon.

Additionally inter configurational charge transfer absorption can take place at the impurity centre when an electron from ligand atom is transferred to  $RE^{3+}$  ion transforming the latter to the 2+ state. These transitions are parity allowed and are energetically usually below 4f–4f<sup>f-1</sup>5d transitions. In many cases they also overlap, making discrimination between the two impossible. When any of the 4f–4f higher level transition is within resonance with the charge transfer band, this configuration relaxes into excited 4f configuration revealing the usual 4f–4f luminescence.

Lifetime of an excited electronic state, e.g. the excited 4f state of the rare-earth ion, is the lifetime, which would be obtained if radiative decay via the unavoidable spontaneous emission was the only mechanism for depopulating the state. It is given by the following equation:

$$\frac{1}{\tau_{rad}} = 8\pi n^2 c \int \frac{\sigma_{em}(\lambda)}{\lambda^4} d\lambda \quad \text{Eq. 1}$$

From the latter it can be concluded that high emission cross sections and a large emission bandwidth ( $d\lambda$ ) inevitably lead to a low radiative lifetime. In rare-earth 4f–4f transitions these entities are rather small (low absorption and narrow line widths of the intraconfigurational transitions) resulting in rather long decays ( $\sim 1$  ms). Ideally the luminescence decay of rare-earth ion's 4f–4f transitions can be described by single exponential law given by:

$$I(t) = I_0 \cdot \exp\left(\frac{-t}{\tau}\right) \quad \text{Eq. 2}$$



When this is true for free ion there are many factors that could change that when luminescence centers are embedded into crystal matrix where inter-ionic interactions as well as interaction with crystal matrix can take place. The effect generally modifies the luminescence decay law by introducing a time dependent function, describing the various interactions:

$$I(t) = I_0 \cdot \exp\left[\frac{-t}{\tau} - W(t)\right] \quad \text{Eq. 3}$$

The exact form of the function is usually hard to find. The most basic interaction between an impurity ion and crystal lattice is the multiphonon relaxation. This always reduces the radiative lifetime of the dopant and depends mostly on the highest phonon energies of the host matrix. According to Weber [36], the number of phonons required to bridge the energy gap of the host must be 5 or more for the multiphonon relaxation to compete with radiative recombination of 4f–4f transitions in semiconductor hosts. This renders zirconia and hafnia good candidates for doping with RE<sup>3+</sup> ions as the corresponding highest phonon energies in them are 650 cm<sup>-1</sup> [37] and 680 cm<sup>-1</sup> [38] respectively. The 4f–4f transition energies of RE ions, especially in the visible, are higher than 12000 cm<sup>-1</sup> resulting in no significant shortening of the luminescence lifetime via multiphonon relaxation.

In case of interionic processes three main interactions between donor (excited) and acceptor (ground state) can take place: energy migration, cross relaxation and upconversion. In the first case two ions of the same kind exchange energy resonantly between the same energy levels allowing effective migration of excitation. The process increases the possibility of trapping the excitation to a defective site where multiphonon relaxation could quench the emission. In case of energy cross relaxation energy from generally higher energy level of the donor excites that of a lower level in acceptor. This leads to a situation where acceptor is excited to a lower overall energy level than that of the donor. As a consequence this process can lead to effective quenching of the excitation when the concentration of the dopants is high [39]. Upconversion process in contrast causes a transition in lower excited state of the donor to promote a higher resonant transition in acceptor. If such conditions exist, then a higher than excitation energy luminescence could effectively be produced [40].

The problem of how the energy exchange takes place between the ions was first studied by Förster and Dexter. Förster proposed that the exchange can happen via dipole-dipole like Coulomb interaction without charge carrier migration from donor to acceptor. Inter-ion distances for typical Förster type interactions are in the few nanometer scale.

According to Dexter at short distances (< 1 nm) where wave function overlap between ions is increased the energy exchange can happen also by charge carrier migration from donor to acceptor. These theories have been

further developed by Inokuti and Hirajama [41]. They propose that in approximation where: donor and acceptor are statistically separated, there exists only one channel for energy transfer and there are no donor-donor interactions or acceptor-donor back transfer,  $W(t)$  can be summarised as:

$$W(t) = \Gamma\left(1 - \frac{3}{s}\right) \cdot \frac{n_a}{C_k} \cdot \left(\frac{t}{\tau}\right)^{\frac{3}{s}} \quad \text{Eq. 4}$$

Here  $\Gamma$  denotes gamma function,  $n_a$  is the acceptor concentration,  $\tau_0$  the radiative lifetime of the donor and  $s$  denotes the interaction multipole order:  $s$  is 6 for dipole-dipole, 8 for dipole-quadrupole and 10 for quadrupole-quadrupole transitions.  $C_k$  is the critical acceptor concentration, at which the Förster-Dexter transfer rate between a donor and an acceptor equals the radiative relaxation rate of the donor.

The apparent (measurable) luminescence decay could further be influenced by inhomogeneous distribution of single exponential decay rates. This so called stretched exponential decay can be expressed as follows [42]:

$$I(t) = \exp\left[-\left(\frac{t}{\tau_0}\right)^\beta\right], \quad 0 < \beta < 1 \quad \text{Eq. 5}$$

Here the parameter  $\beta$  represents system dependent factor that describes the distribution of single exponential decay rates. Such inhomogeneity can arise from many different factors. Generally it is believed to originate from charge carrier de-trapping to non-localised states or hopping between localized states in crystal. The trap depths are considered having a distribution rather than discrete values arising primarily from nanocrystallite size differences or different surface states where excitons can localise. The average decay rate of such system can be derived as:

$$\langle \tau \rangle = \tau_0 \Gamma(1 + \beta^{-1}) \quad \text{Eq. 6}$$

In the limiting case when  $\beta \rightarrow 1$  the normal exponential decay law is derived from the above. In many complex solids this is not the case and lower values of  $\beta$  are observed [42 and references therein].

## 2.5. Rare-earth ions as phase stabilisers

Phase stabilisation of high temperature tetragonal and cubic phases of zirconia and hafnia is generally achieved via doping the crystal lattice with aliovalent metal ions with slightly different ionic radii. This process introduces disturbances and oxygen vacancies into crystal lattice which create various thermodynamic barriers to prevent the crystal from relaxing into equilibrium at room temperature. Historically most successful dopant used for such purpose has been yttrium. A generally agreed phase diagram picture in Figure 1 represents the approximate yttrium molar concentration needed for stabilisation of different zirconia metastable phases.

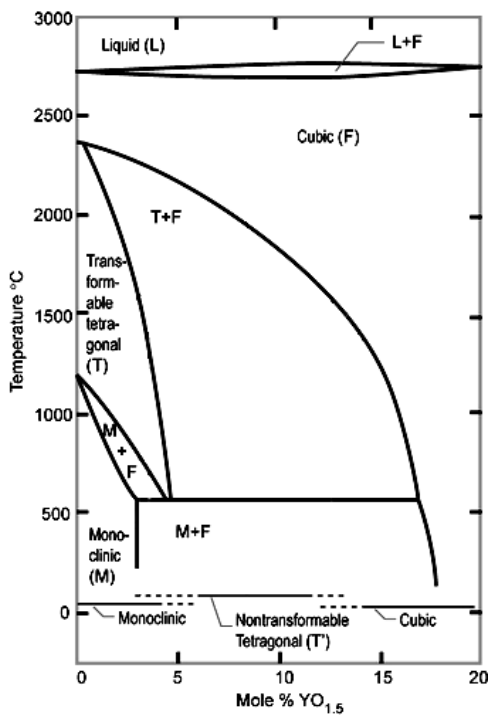
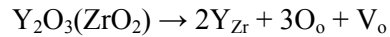


**Figure 1:** Phase diagram of zirconia-yttria solid solution at different temperatures [18].

As seen from the data the approximate minimal molar ratios of yttrium for RT stabilising tetragonal and cubic phases are around 5 mol% and 12 mol% respectively. It has been suggested that the main contributor to phase stabilisation are the introduced oxygen vacancies as opposed to the dopant ions [43,44]. Statistically for every 2 dopant atom one oxygen vacancy is created:



In many of the technological and scientific applications nanocrystalline forms of the oxides are used instead of bulk. In works describing nanocrystalline (powder form) zirconia and hafnia the yttrium molar values reported for phase stabilisation are usually lower. The reduction in needed dopant concentration is related to

the additional effect of surface energy that becomes important as the crystallite surface-volume ratio becomes high. Generally the formation of stable monoclinic phase is thermodynamically controlled by Gibbs free energy shrink in tetragonal to monoglinic (t-m) transition (generally also in cubic to tetragonal (c-t) transition). To account for all relevant factors the free energy change  $dG$  in phase transition can be summarised as follows [45,46]:

$$dG = dG_{chem} + dW + dW_{stress} + dS \quad \text{Eq. 7}$$

Here  $dG_{chem}$  represents the chemical free energy difference,  $dW$  energy barrier related to the stresses caused by surrounding matrix to the zirconia nanocrystals and  $dW_{stress}$  the energy barrier caused by the forces exerted by the macroscopic shear forces. Latter is caused either by strains caused by crystal growth or from external sources. Term  $dS$  denotes the change in free energy of the surface area of the nanocrystallite.

Naturally for the transition to happen we assume that  $dG_{chem} < 0$ . In this case the other terms of Eq. 7 must not exceed its absolute value to allow  $dG < 0$ . In case of t-m transition the term  $dW_{stress}$  has always a positive value because of the higher cell volume of monoclinic phase. The formation of monoclinic phase leads to extensive production of twin crystals [46] (e.g. formation of new surfaces for divided nanocrystals that don't fit to the old volume). Therefore the term  $dS$  can be divided into two different parts:

$$dS = dS_{t-m} + dS_{twin} \quad \text{Eq. 8}$$

Here the first term describes the surface energy change and the second term the additional energy needed for creating a twin boundary between divided crystals. The additional twin energy tends to render the total  $dS$  to be a positive value.

These restrictions play an important role in stabilising the higher temperature tetragonal phase when the crystals are small in diameter. Successful stabilisation of cubic form has often been achieved at as low as 8 mol% [43] in both oxides. For tetragonal phase only a few mol% addition of yttrium has been reported to be enough [43,44].

Yttrium is very similar in its ionic radii to the rest of the lanthanoids. Therefore it is natural to assume that other lanthanides could be as effective in stabilising metastable tetragonal and cubic structures. Respective results shown by Zhang et. al. indicate that by doping zirconia with 8 mol% of different lanthanoid species cubic phase could be stabilised [47]. Similar results have been shown for cubic hafnia at 10–20 mol% [48,49].

Technological interest in controlling the conditions for phase stabilisation is great because of better dielectrical properties of especially the tetragonal phase. Dielectric constant of  $k \sim 38$  have been demonstrated lately in germanium stabilised tetragonal zirconia rendering it a very good candidate for future gate dielectric in semiconductor industry [50].

### 3. SAMPLE PREPARATION

#### 3.1. Introduction

For preparing  $\text{ZrO}_2$  and  $\text{HfO}_2$  samples with different defect and impurity composition several preparation techniques were chosen. ALD was selected for producing film samples with high crystalline quality. The samples were used for comparison with theoretical calculations as well as used for studying the effect of defect creation via ion implantation of RE ions.

As a direct opposite – sol-gel technique was chosen to prepare highly defective and porous samples with in situ chemical doping of RE ions for studying dopant emission properties and phase stabilization of the oxides. Despite the defectiveness, sol-gel technique enabled variety of macroscopic modifications of the materials to be produced. In the present work either nano-powder, thin film or special micro-rolled form of the oxides are studied.

Skull-melting technique was used for producing bulk samples of high quality to study the effects of RE concentration and phase composition to the PL properties.

In the next paragraph an overview will be given about each of these methods in terms of their technological details as well as the main characteristics of the materials produced by the respective techniques. A detailed description of preparation and basic properties of the samples used in the following optical and spectroscopic investigation will be given.

#### 3.2. ALD process

ALD is a form of chemical vapour deposition (CVD) introduced in 1974 by T. Suntola originally to improve the quality of ZnS films [51]. This method was intensively developed and elaborated at Institute of Physics, Tartu since 1990 by J. Aarik [52]. The main difference with CVD process is that in ALD the precursor materials are kept separate and applied in consecutive steps. In the simplest case ALD process uses two precursor materials which are alternately exposed to the growth surface with intermittent purge with a purge gas (usually  $\text{N}_2$ ) [52]. These basic steps can be visualised as shown on Figure 2.

The ALD process starts with a precursor pulse containing appropriate metal precursor (step a). After saturation the excess precursor molecules are purged (step b). Now oxygen carrying precursor is introduced which forms respective metal oxide monolayer (step c). Finally the by-products and excess precursor are removed by the second purge (step d).

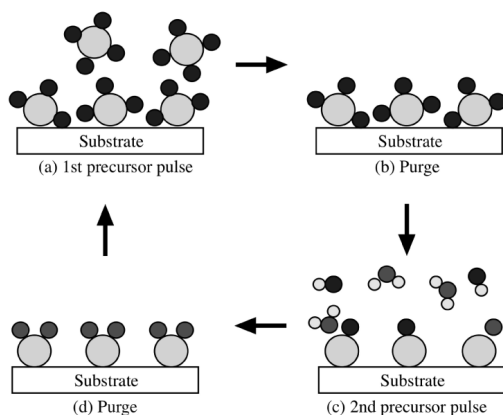


**Figure 2:** Basic steps of ALD process.

In order to maintain high quality of the ALD deposited materials the precursor materials need to be chosen so that their vapour pressure is sufficiently high to prevent excessive condensation (more than one atomic layer) of the precursor material. For transition metal oxides ( $\text{TiO}_2$ ,  $\text{ZrO}_2$  and  $\text{HfO}_2$ ) the most studied precursors are metal-tetra-chlorides of the respective metal ions ( $\text{TiCl}_4$ ,  $\text{ZrCl}_4$  and  $\text{HfCl}_4$ ) [53]. Additionally metal-tetra-iodine precursors have shown promising results ( $\text{TiI}_4$ ,  $\text{ZrI}_4$  and  $\text{HfI}_4$ ) [54]. Commonly used oxygen precursors for chloride and iodine based processes are water vapour ( $\text{H}_2\text{O}$ ) or hydrogen peroxide ( $\text{H}_2\text{O}_2$ ) respectively [52].

ALD is a self-limiting adsorption reaction process, i.e. the amount of deposited precursor molecules is determined only by the number of reactive surface sites and is independent of the precursor exposure after saturation. In theory, the maximum growth rate is exactly one monolayer per cycle, however in most cases the growth rate is limited to 0.25–0.3 of a monolayer [52].

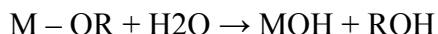
For monitoring the exact thickness (in units of atomic layers) of the film the samples are grown on a quartz crystal microbalance (QCM) sensor crystal which changes its oscillation period according to deposited sample mass [55]. After appropriate calibration the mass change can be used for estimating the absolute absorbed precursor amount and hence estimate the final thickness of the film in atomic layer precision [52,55].

### 3.3. Sol-gel process

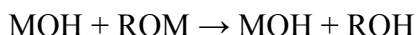
The sol-gel process is the process of sol's transition to gel (gelation). It is often used as a part of wet chemical techniques. It is widely used in the field of materials science for producing metal oxide ceramics. Sol-gel process generally involves the use of inorganic salts or metal alkoxides as neat materials.

Hydrolysis and polycondensation reactions occur when materials are mixed with water (and catalyst).

In general the reactions taking place in sol-gel process can be summarised in two steps. First, a mixture of precursor, water and catalyst is prepared in appropriate concentration ratios. As a result hydrolysis takes place to form “sol”:



Here M is appropriate metal (Si, Ti, Zr, Hf, etc.) and R is an alkyl group (e.g. CH<sub>3</sub>, C<sub>2</sub>H<sub>5</sub>, etc.) [56,57]. In the next step condensation occurs in the solution:



As these reactions proceed oxopolymers and eventually hydrous metal oxides form when excess water is added [58]. The latter species combine (condense) into a network of M-O-M bonds with different branching lengths and varying dimensionality as solvent is slowly removed. The semi viscous solution is referred to as “gel” because of its increased viscosity compared to “sol”.

By altering the reaction conditions (temperature, concentration, pH, solvent and reactant), the degree and nature of the condensation reactions can be controlled. At low pH conditions the rate of condensation slows down the degree of branching resulting in low cross-link density and very porous gels. In contrast high pH will cause rapid condensation that can produce dense particles that precipitate from the solution. In conjunction with controlled drying of the gel, the porosity and composition of the products can be tuned. For example highly porous materials (xerogels) can be produced that are exceptional thermal insulators [59]. Dense thin gel films are used as protective coatings on lenses or refractory surfaces. Porous thin films and dense nanoscale powders are used in sensor applications [60].

Additional advantages of sol-gel process compared to numerous other material growth methods are: need for relatively low ambient temperature, possibility to dope the material with foreign molecules in-situ and the ability to precisely control the macroscopic shape of the material during the gelation stage.

Tip-coating and spin coating methods can be used for covering substrates of marginal sizes up to square meters in industrial solutions (less in spin-coating). In both technologies first the sol is applied to the surface of the substrate, evenly spread over the coverable area and finally dried to remove the excess solvent. The two processes differ mainly by the way the sol is applied to the surface. In tip-coating the substrate is immersed to the sol and slowly risen out. The final thickness of the tip-coated sol layer is therefore governed mainly by viscous and gravitational forces. Spin coating accomplishes the same by spreading a small

amount of sol placed at the centre of the substrate radially by centrifugal forces caused by high speed spinning of the substrate (typically 1000–4000 rpm).

When covering a pre-determined surface area is not the goal – rather different techniques can be applied for producing standalone sol-gel particles. Recently a promising new technology has been developed by V. Reedo et. al. [61] for creating sol-gel microrolls.

The process starts with preparation of a sol in the usual manner. In gelation stage instead of forced shaping into thin film or other shapes a self-induced structuring of the gel is used for forming the microrolls. In a confined container gelation of the sol starts from the surface with the gelation gradient directed into the sol. When solvent is added significant amount of the underlying sol layer below already gelled surface can be dissolved. As a result freestanding gel film segments form and roll spontaneously into microscopic rolls of alkoxide gel. This is caused by the shrinkage of sol's surface, which exerts forces on the upper layer of the gel segments. By controlling the gelation time before solvent introduction and the humid air introduction rate the thickness and dimensions of the gel sheets can be varied leading to ability of manipulating the forming roll diameter and size (number of gel layers in a roll).

### **3.4. Skull melting process**

Directional solidification of melts is a powerful method for growing macroscopic single- and polycrystalline materials in macroscopic quantities. The method involves formation of a melt of the starting materials followed by controlled (usually directional) cooling. Many oxides and metals do melt at fairly high temperatures making finding suitable crucible for containing their melts difficult. Skull-melting is techniques overcoming this obstacle. In skull-melting the starting materials are contained within a water cooled crucible that forms (due to rapid thermal energy conduction) a cooled and therefore solidified “skull” of the molten material outside the high temperature melt [62].

The melting of the starting materials is usually achieved by radio frequency (RF) heating. In order to let maximum amount of RF energy into the crucible the skull-melting crucible is constructed out of closely spaced rods or fingers which are internally water-cooled. The RF-melting process is induction based which means that the starting materials must conduct electricity to build up heat. Many insulating materials such as oxides, carbides and nitrides do not couple to the RF fields. To melt an insulating oxide, a graphite ring or disk is placed in the crucible for initial coupling with the RF field (high temperature melts usually couple well). If the reaction is run under air, the graphite burns away and thus does not contaminate the sample. When a high temperature melt is established it is cooled slowly to room temperature. The latter is usually done directionally for ensuring the formation of mono-crystals in the centre of the melt [59]



Skull-melting is readily used for producing industrial amounts cubic zirconia for gemstone industry [63]. In-situ doping of various oxides via mixing dopants into the starting materials of the melt has successfully been employed [64,65].

### 3.5. Ion implantation

Ion implantation is a method for doping various types of materials via high energy ion bombardment. Its advantages over other in-situ chemical and physical doping methods are: very good control over dopant concentration, control over spatial distribution of dopants, very high possible dopant doses and non-dependability from chemical and physical incompatibilities between dopant and target material.

Ion-implantation is industrially used for doping of semiconductors with p or n type impurities and for doping of metal surfaces with suitable ions for improving surface resistance to wear and friction [66].

Technically ion-implantation begins with forming gaseous plasma of dopant ions. Ionized plasma is accelerated in electric field, passed through a bending magnet for mass separation and given final acceleration before hitting the target. Ions are typically accelerated from 10 up to 500 keV.

The forces acting on the deceleration of ion with energy  $E$  in matter can be characterized via stopping power  $S(E) = -\frac{dE}{dx}$ . Main contributions to the

latter are electronic and atomic stopping powers. At the beginning of the deceleration, when the energy of the ion is still high the prevalent force acting on the ion is electronic in nature. Inelastic collisions with target medium electron field cause numerous ionizations both in target and of the ion. Therefore the initial ionization level and final ionization state are usually not linked as the ions go through many different ionization stages before stopping.

At lower energies at the end of the penetration path ions tend to collide also with repulsive potentials of the target atoms. These collisions are elastic and cause atoms to drift from their equilibrium positions. This causes numerous secondary collision cascades among target atoms thus producing relatively more damage than electronic stopping. Also the trajectory of the ions tends to change significantly more in atomic stopping region.

To account for both forces the resultant stopping force is denoted as the combination of the two:

$$S(E) = -\left(\frac{dE}{dx}\right)_{nuclear} - \left(\frac{dE}{dx}\right)_{electronic} \quad \text{Eq. 9}$$

The expected range ( $R_p$ ) of an ion can be estimated from the latter as an integral over the total energy loss [67]:

$$R_p = \int_0^E \frac{dE}{\left(\frac{dE}{dx}\right)_{nuclear} + \left(\frac{dE}{dx}\right)_{electronic}} \quad \text{Eq. 10}$$

For N ion system the deviation from the  $R_p$  is probabilistic and therefore in the simplest approximation results in Gaussian shaped profile around  $R_p$ .

In real systems the depth and concentration distribution of the ions depend heavily on the ion energy and type of target and source atoms introducing factors like asymmetry of the profile (skewness) and flatness of the peak (kurtosis). These modifications become important as the initial energy and mass of the ions increases resulting in a more complicated shape of the distribution. A good fit to experimental data has been achieved when a Pearson approximation is used that takes into account all the factors [68].

As the base knowledge of the underlying processes of stopping of the ions is well known the most used method for determining approximate distribution of ions in real systems is often numerical Monte-Carlo type simulation instead of experimental methods. A widely accepted code for such simulations is TRIM (Transport of Ions In Matter) on which numerous software implementations have been created [69]. When TRIM simulation data is compared to Pearson approximation (see Figure 3) a relatively good fit can be obtained. The actual calculations in current case were performed with a freely available software package SRIM [70] which is based on the TRIM code.

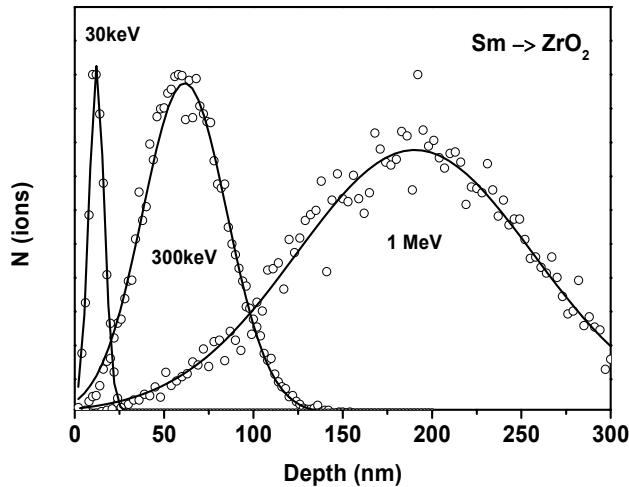


**Figure 3:** Example of final ion distribution profiles in  $ZrO_2$  implanted with Sm ions at various acceleration energies. The datasets (dots) are derived from SRIM [70] software simulation and fitted (solid lines) with PearsonVII approximation.

### 3.6. Overview of prepared zirconia and hafnia samples

The ALD prepared samples were grown in cyclic chloride based ALD process on silicon substrate [71]. The thickness of the prepared  $\text{ZrO}_2$  and  $\text{HfO}_2$  samples was  $\sim 200$  nm. Phase content of the samples in as-grown state was confirmed by reflection high energy electron diffraction (RHEED) and XRD measurements to be mostly monoclinic in  $\text{HfO}_2$  and a mixture of monoclinic and tetragonal in  $\text{ZrO}_2$ . After initial growth the samples were implanted with 300 keV Eu and Er ions up to dose  $\sim 10^{14}$  ions/cm<sup>2</sup>. To re-establish the crystalline structure the samples were annealed in air in 15 minutes cycles from 400°C to 1100°C at 100°C steps.

Sol-gel prepared  $\text{HfO}_2$  samples were prepared via sol-gel route proceeding from  $\text{Hf}(\text{OBU})_4$ . The synthesis started from polymerizing  $\text{Hf}(\text{OBU})_4$  in 45% hexane solution and by subsequent adding of water in molar ratio 1:1.6. Doping the material with Sm, Eu and Tb ions was accomplished by dissolving 0.5–1% of respective metal chlorides in the sol. Estimated final concentrations of the dopants were in the range from 0.3–0.4 mol%. Forming doped oxide thin films was achieved via applying the prepared sol to quartz substrates using tip-coating technique. All samples were finally annealed in air for 1h at 800°C for obtaining crystalline structure.

For sol-gel preparation of hafnia powders 1.5 g of dry 1-butanol (refluxed over  $\text{CaH}_2$  for 1 h and distilled before use) was mixed with 1.0 g of 45% hafnium(IV) 1-butoxide solution in hexane. In order to induce the initial oligomerisation of the alkoxide, 0.0137 g of concentrated HCl dissolved in 3.0 g of 1-butanol (water and alkoxide molar ratio  $R=0.5$ ) was added drop wise into the vigorously stirred solution. Finally, the solution was concentrated by evacuating solvents into vacuum with Büschi rotator evaporator. The obtained solventless viscous (honey-like) substance was left for aging in Petri dishes at ambient conditions for a week for final polymerization and release of organics. After aging, the obtained powder was annealed in air up to 1000°C maximum.

A modified sol-gel route was used for preparing Sm doped  $\text{ZrO}_2$  micorolls. In this case partial polymerization of  $\text{Hf}(\text{OBU})_4$  was carried out by adding 1.36 ml of butanol solution containing 1.7% water, 0.45% HCl and 0.95%  $\text{SmCl}_3 \cdot 6\text{H}_2\text{O}$  to 1.5 ml of  $\text{Hf}(\text{OBU})_4$  (80 wt% in 1-butanol). Solution was rotated and air evacuated in a flask placed into a 80°C water bath to evaporate the solvent (butanol). Thereby an even layer of non-flowing sol was obtained on the inner surface of the flask.

The spontaneous rolling of the non-flowing sol was initiated by the formation of gradient of gelation extent in the sol exposed to high humidity air that was introduced into the flask for 1 minute cycles. In the next stage free-standing film segments were obtained via adding hexane solvent to the flask which dissolved the underlying sol layer. Obtained freestanding film segments rolled spontaneously into microscopic rolls as described in Chapter 3.3.

Remaining sol was removed by several cycles of diluting and decanting [61]. The formed zirconia microrolls contained  $\sim 0.5$  mol% samarium. For investigation of the dynamics of crystallographic phase formation the obtained samples were annealed in air at 500, 600, 700 and 800°C.

Bulk samples of  $\text{ZrO}_2$  were grown by directional solidification of melt technique using RF heating in water cooled crucible. The growth of the crystal was performed with Kristall-407 melting equipment. The cold container with 130 mm diameter was used for gradual 10 mm/h growth of the crystals. After initial heat-up the cooling rates of the melt were 180–200°C/min at above 1000°C and 30°C/min in between 500–1000°C. The resulting crystals were 16–60 mm in length and 5 to 20 mm in diameter (after removal of the formed skull). The samples with  $\text{ZrO}_2 + x \cdot \text{Sm}_2\text{O}_3$  ( $x=8\%$  and  $10\%$ ) were transparent bulk materials with light brown tint. The sample with 4 mol% of samarium concentration appeared opaque and milky in colour. Preliminary XRD measurements of the samples revealed that the 10 % doped sample contains mixture of tetragonal and cubic phases. The 8 % doped sample is nearly 100% tetragonal and the 4 mol% doped sample contains mixture of monoclinic and tetragonal phases.

For further studies the 4 mol% samples were cut into 1 mm thick slabs by diamond saw. In case of the 8 and 10 mol% samples physically cracked surfaces were used.

The samples investigated in scope of present thesis are listed in table 1:

**Table 1:** Basic properties of prepared  $\text{ZrO}_2$  and  $\text{HfO}_2$  samples.

<i>Chemical notation (host:dopant)</i>	<i>Preparation technique</i>	<i>Crystal morphology*</i>	<i>Heat treatment (max, °C)</i>	<i>Dopant concentration</i>
$\text{HfO}_2$	sol-gel precipitation	m	1000	–
$\text{ZrO}_2$	ALD	m	–	–
$\text{HfO}_2$	ALD	m	–	–
$\text{ZrO}_2:\text{Er}^{3+}$	ALD	m	1100	0.07 at%
$\text{ZrO}_2:\text{Eu}^{3+}$	ALD	m	1100	0.07 at%
$\text{HfO}_2:\text{Er}^{3+}$	ALD	m	1100	0.07 at%
$\text{HfO}_2:\text{Eu}^{3+}$	ALD	m	1100	0.07 at%
$\text{HfO}_2:\text{Sm}^{3+}$	sol-gel	m	800	0.3–0.4 mol%
$\text{HfO}_2:\text{Eu}^{3+}$	sol-gel	m	800	0.3–0.4 mol%
$\text{HfO}_2:\text{Tb}^{3+}$	sol-gel	m	800	0.3–0.4 mol%
$\text{ZrO}_2:\text{Sm}^{3+}$	sol-gel micro rolling	t+m	800	0.5 mol%
$\text{ZrO}_2:\text{Sm}^{3+}$	skull melting	t+m	> 2700	4 mol%
$\text{ZrO}_2:\text{Sm}^{3+}$	skull melting	t	> 2700	8 mol%
$\text{ZrO}_2:\text{Sm}^{3+}$	skull melting	c	> 2700	10 mol%

\* Crystal phases are denoted as: m – monoclinic; t – tetragonal; c – cubic

## **4. SPECTROSCOPIC INVESTIGATION OF RE<sup>3+</sup> DOPED ZrO<sub>2</sub> AND HfO<sub>2</sub> [PAPERS I–V]**

### **4.1. Introduction**

ZrO<sub>2</sub> and HfO<sub>2</sub> can be prepared via many different routes in addition the techniques covered in present work. Different methods usually introduce different amounts and types of defects and in conjunction with macroscopic shape and dimensions of the materials result in wide deviation in PL, conductivity as well as other intrinsic properties. Because of the relatively wide band-gap, ZrO<sub>2</sub> and HfO<sub>2</sub> can be combined with great variety of extrinsic luminescence centers which introduce another degree of freedom for describing their excitation and PL properties.

Some of the PL related properties are rather well documented by now. These include band-gap, existence of STE states and for example RE related charge transfer absorption. Nevertheless despite generally similar emission properties of RE related centers, wider disagreement exists in describing the excitation mechanisms of the latter as well as many intrinsic defect related phenomena.

In an attempt to add understanding into the various processes involved the following spectroscopic study of PL emission properties will try to cover as wide as possible selection of differently prepared and dopant activated ZrO<sub>2</sub> and HfO<sub>2</sub>.

The experimental work focuses first on describing the intrinsic band structure on the basis of ALD prepare samples. As ALD yields theoretically the purest crystal structure the optical properties from the latter samples are compared to theoretical predictions from DOS calculations.

In the proceeding chapters the effect of RE<sup>3+</sup> doping will be discussed. Main objectives will be the characterization of the energy transfer process as well as the energy level placement of the Er, Eu, Sm and Tb dopant ions relative to the host band states. Different scenarios will be discussed depending on the host-dopant selection.

The discussion is not exactly following the chronological sequence of supporting papers presented in appendix but rather present a summary of the earlier findings with the addition of several new results. The discussion is divided into chapters describing the main information gained from separate investigation of the materials prepared by ALD, sol-gel and skull melting techniques followed by a more general discussion about the decay dynamics. Finally a tentative energy level structure of the systems is proposed.

## 4.2. Experimental setup

The PL measurements of the samples were carried out mainly on two setups. Measurements with excitation energies below the air absorption edge ( $< 6$  eV) were carried out on a back-scattering setup at ambient pressure either in air or in He environment in bath-type Utreks type cryostat, used for achieving low temperatures (down to 6 K).

Luminescence excitation was carried out using fixed energy ArF excimer laser (6.42 eV, 2 ns pulses with 30 Hz repetition rate), 150 W Xenon lamp (dispersed through MDR-23 type monochromator) and variable wavelength two stage OPO from Ekspla Ltd. (10 ns,  $\sim 20$   $\mu$ J pulses with 20 Hz repetition rate). The pulse energy of the OPO was highly fluctuation from pulse to pulse as well as depending on output energy because of the nonlinear response of the OPO stages.

Luminescence spectra and excitation spectra were recorded by a computer controlled Andor SR-303i spectrograph equipped with Andor ICCD camera (type DH-501). Excitation spectra and decay kinetics were recorded with Hamamtsu photon counting photomultiplier head (type H8259-01) coupled with multichannel analyser (type P7882, FAST ComTec).

Measurements at excitation energies exceeding air absorption edge were carried out at beamline “I” of the Hasylab synchrotron radiation laboratory at Desy (Hamburg, Germany). Energies in the range from 3.7 to 20 eV were available at pulse cycle intervals of 192 ns. The samples were placed in a high vacuum ( $10^{-9}$  mbar) environment. Low temperature measurements were carried out with the aid of a flow type cryostat permitting stable temperature control of the sample holder down to 10K. The photoluminescence signal was registered with VUV monochromator (type Spectra Pro 300i) equipped with Princeton Instruments liquid nitrogen cooled CCD detector. The excitation spectra were recorded with photo multiplier tube (type R6258P). All excitation experiments at beamline “I” were controlled by in-house built controller software (LabView).

To gain better understanding of experimental spectroscopic data, a number of physical properties of  $\text{ZrO}_2$  were calculated using the DFT based ab initio methods. The list of the calculated properties is as follows: theoretical band structure, total and partial DOS and optical properties (dielectric function, absorption, refractive index). The calculations were performed for the ideal crystal lattice and for the crystal lattice with oxygen vacancies. The CASTEP module of the Materials Studio 4.0 developed by Accelrys [72,73] was employed in the calculations. The CASTEP module was based on total plane-wave pseudopotential method.

### 4.3. Undoped sol-gel and ALD prepared films [papers I,II,IV]

Under higher than band-gap excitation energies the pure ALD prepared  $\text{ZrO}_2$  and  $\text{HfO}_2$  samples revealed broad emission bands around 4.1–4.3 eV at 10 K (see Figure 4 left). At RT the PL emission is quenched in  $\text{ZrO}_2$  and weakly present in  $\text{HfO}_2$ . According to Kirm et. al. these emission bands have been observed in  $\text{ZrO}_2$  and  $\text{HfO}_2$  at 4.2 and 4.4 eV and regarded as intrinsic STE recombination bands in both [19]. From photoluminescence excitation spectra (see Figure 4 right) it is evident that efficient excitation of the STE bands starts rather sharply at 5.3 eV and 5.8 eV for  $\text{ZrO}_2$  and  $\text{HfO}_2$  respectively. These sharp peaks are according to Kirm et. al. the exciton absorption bands laying just below the conduction band minimum. Further increase of the excitation is steadier, reaching up to  $\sim 6.5$ – $7.0$  eV. Direct band-gap values derived from the power law  $((Ih\nu)^2 \text{ vs. } h\nu)$  plot in that region (see Figure 5) are 5.58 eV for  $\text{ZrO}_2$  and 6.15 eV for  $\text{HfO}_2$ .

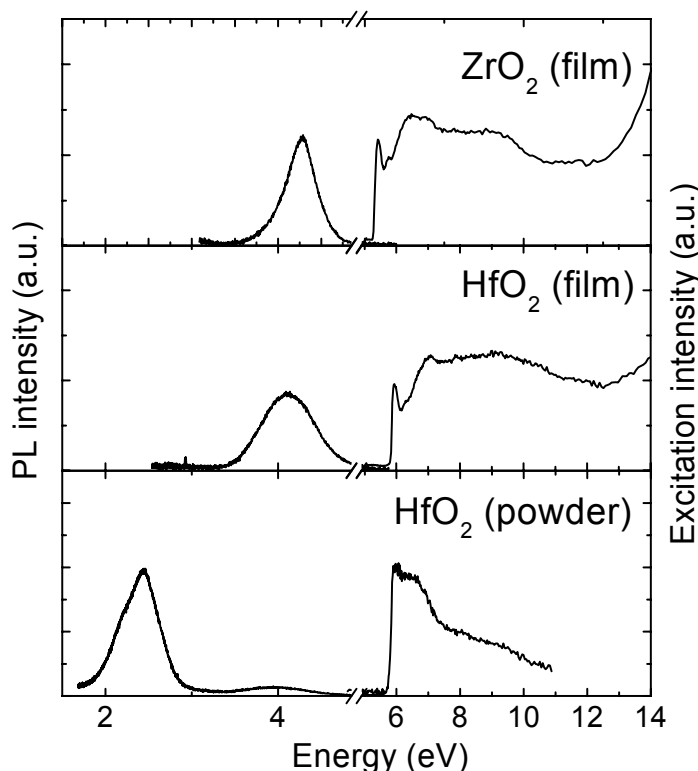


**Figure 4:** PL emission (left) and excitation (right) spectra of ALD prepared  $\text{ZrO}_2$  and  $\text{HfO}_2$  films compared with that of the  $\text{HfO}_2$  powder. Excitation spectra are registered at the respective maximas of the below 5 eV PL emission bands in all samples.

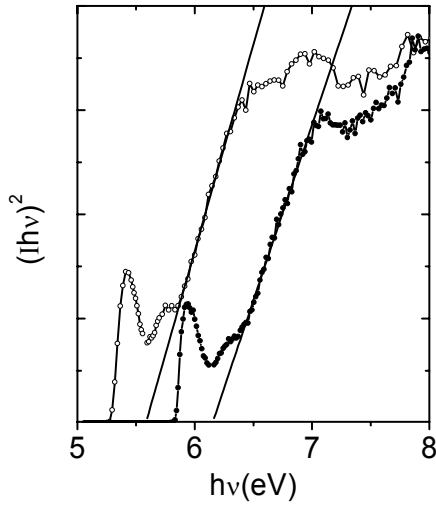


**Figure 5:** Absorption edges of  $\text{ZrO}_2$  (circles) and  $\text{HfO}_2$  (filled circles) derived from intrinsic PL excitation data in power law plot.

$\text{ZrO}_2$  start at  $> 5$  eV and extends by forming a continuous band up to  $\sim 17$  eV. This is in good agreement with experiment and previous theoretical work by L. K. Dash et. al. [20] where the conduction band was observed to stretch from  $\sim 5.3$  eV to rather similar 18.5 eV.

In sol-gel prepared  $\text{HfO}_2$  powder the STE emission (at 10 K) was very weak and slightly red shifted (by  $\sim 0.1$  eV). Additionally a strong defect related emission band centered at 2.7 eV emerged. Most noticeable difference in excitation spectra of the VUV band was the reduction in efficiency beyond  $\sim 7.0$  eV.

It is believed that such changes in PL and excitation are caused primarily by introduction of oxygen vacancies in both  $\text{ZrO}_2$  and  $\text{HfO}_2$ .

The CASTEP calculated absorption spectra of an undoped  $\text{ZrO}_2$  bulk crystal (see Figure 6) show that the conduction band absorption in

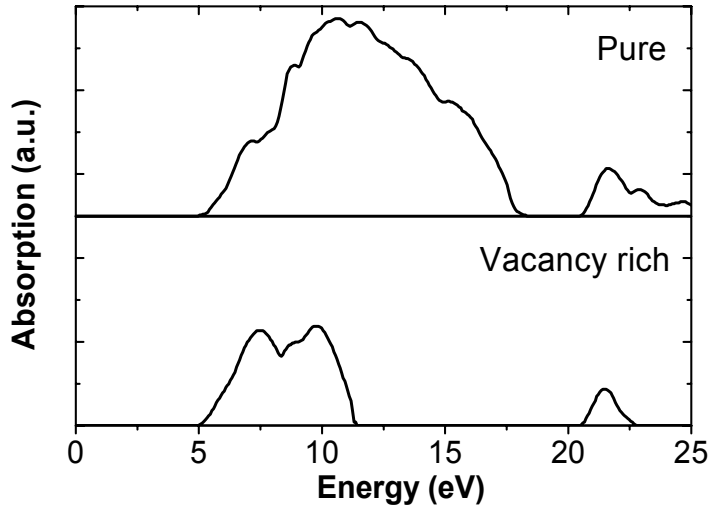


**Figure 6:** Calculated absorption spectrum of ideal “pure” and oxygen vacancy rich  $\text{ZrO}_2$ .



When oxygen vacancies are introduced into the same model the calculated absorption spectra is changed considerably and shows narrowing of conduction band down to width of about 2–3 eV (see Figure 6). A similar reduction was also seen in highly oxygen vacancy rich (due to need for charge compensation)  $\text{RE}^{3+}$  implanted ALD prepared  $\text{HfO}_2$  films. The extended excitation spectra of STE luminescence on Figure 7 of  $\text{Eu}^{3+}$  implanted  $\text{HfO}_2$  film shows similar drop in excitation efficiency beyond 7 eV, which also can serve as an indication of the conduction band narrowing.

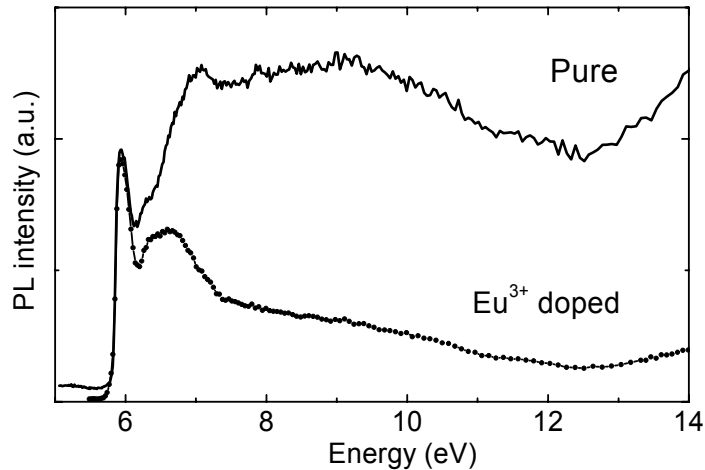


**Figure 7:** Excitation of intrinsic PL (at 3.74 eV) measured in as-prepared “pure” and  $\text{Eu}^{3+}$  implanted and at 600°C annealed  $\text{HfO}_2$  samples.

It must be noted that in case of excitation spectra measurements total similarity with theoretical calculations is not expected. The residual absorption in the region  $> 10$  eV in the experimental spectra is probably caused by two photon emission starting from double band-gap value  $\sim 5$  eV. Additionally different defect related absorption processes not accounted for in theoretical calculations can cause additional non-zero absorption. Based on the latter assumptions it can be concluded that in general a very good agreement between theoretical and experimental results on absorption/excitation spectra of  $\text{ZrO}_2$  has been found and considerable reduction in conduction band width from  $\sim 10$  eV to  $\sim 2\text{--}3$  eV is proposed to be caused by oxygen vacancies in  $\text{ZrO}_2$  and  $\text{HfO}_2$ .

#### 4.4. Ion implanted ALD films [paper I]

Ion implantation is known to introduce large amount of defects (including oxygen vacancies as shown in previous chapter) and cause amorphisation of the target to a large extent. In case of ALD prepared  $\text{ZrO}_2$  and  $\text{HfO}_2$  films the latter manifested as total absence of luminescence in as-implanted samples. The luminescence features were recovered only after gradual annealing in several steps (see Figure 8). Starting from annealing temperature of  $600^\circ\text{C}$  the Eu and Er ions clearly revealed typical 4f-4f transitions' luminescence features in both oxides when band-to-band excitation was employed (6.4 eV). The luminescence intensity increased during annealing (see insets Figure 8) caused by gradual rebuilding of the damaged (due to ion implantation) crystal structure. The exceptional decrease in PL output at  $1100^\circ\text{C}$  in case of Er in  $\text{ZrO}_2$  is believed to be caused by the t-m phase transition resulting substantial amount of Er ions being placed in surface sites not favourable for efficient energy transfer from the host (see further discussions in paper II).

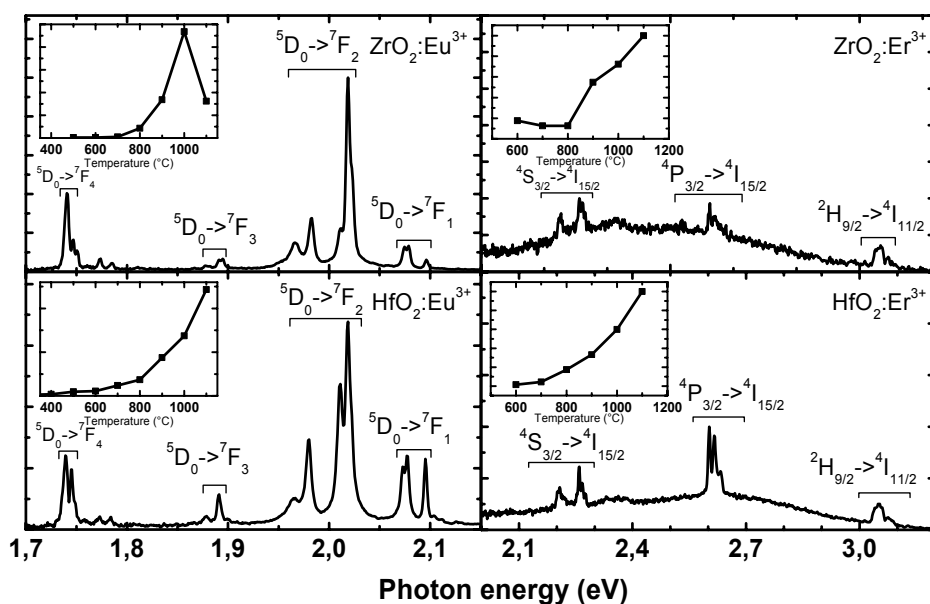


**Figure 8:** PL spectra of  $\text{Eu}^{3+}$  and  $\text{Er}^{3+}$  doped  $\text{ZrO}_2$  and  $\text{HfO}_2$ . The PL intensity increase during annealing cycle indicated on insets.

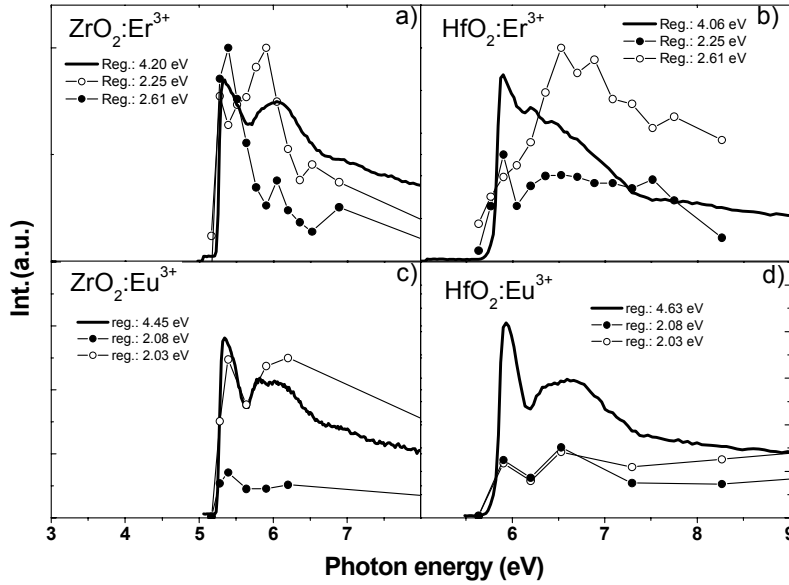


**Figure 9:** Excitation spectra of intrinsic and dopant emission in  $\text{ZrO}_2$  and  $\text{HfO}_2$ . Solid curves indicate intrinsic, dotted curves respective dopant emission excitation.

When the excitation of the  $\text{Eu}^{3+}$  and  $\text{Er}^{3+}$  photoluminescence is observed a good correlation with exciton luminescence is found. In both oxides the excitation of the  $\text{Eu}^{3+}$  ions emission follows the principal band-gap structure as well as exciton absorption (see Figure 9) indicating efficient energy transfer from the host via STE states or some defect sites populated via STE absorption.

Similar behaviour is seen in excitation of  $\text{Er}^{3+}$  4f–4f luminescence with an exception being the  $^2\text{P}_{3/2} - ^4\text{I}_{11/2}$  transition at 2.25 eV. As can be seen the excitation spectra of the latter does not follow that of the exciton absorption and reaches maximum later in conduction band of the host.

The different behaviour can be related to the different energy needed for 4f intra shell excitation of the electron from the  $\text{Er}^{3+}$  ground state ( $^4\text{I}_{15/2}$ ) to the luminous terms. For  $^2\text{S}_{3/2}$  term this energy is 2.28 eV and 3.9 eV for  $^2\text{P}_{3/2}$ . Significant difference between the energies means that the energy transfer from the host is localised in different type of sites. As the excitation of  $^2\text{P}_{3/2}$  term does not follow the exciton absorption the intermediate state for energy transfer cannot be STE state. This is supported by the fact that despite large Stokes shift STE emission resides at slightly higher energies ( $> 4.0$  eV, see Figure 4) and that the STE emission is noticeably quenched at RT whereas  $\text{Er}^{3+}$  emission does not seem to depend on it. As a result some higher laying defect states must be considered.

Dominant localised levels within band-gap of  $\text{ZrO}_2$  and  $\text{HfO}_2$  are oxygen vacancies at various charge states. In theoretical calculations numerous states

have been identified with charge states ranging from  $V_{2+}$  to  $V_{2-}$  as shallow electron traps below conduction band to deep mid gap occupied states [74,75]. Best match for  $^2P_{3/2}$  term excitation could be according to the observations be some of the singly  $V_{-}$  or doubly charged  $V_{2-}$  vacancies presenting rather deep electron traps at 2.2 or 1.6 eV below  $ZrO_2$  conduction band [74]. Similar states have also been observed in experimental studies by C. Morant conducted on  $Ar^{+}$  implanted  $ZrO_2$  [76]. Defect emission around 3.8 eV found in the latter work was identified as oxygen double vacancy.

Ultimately it is rather difficult to identify the exact traps responsible for the energy transfer as for example  $Er^{3+}$  ion can easily be excited to higher  $^4D_{5/2}$  or  $^4D_{7/2}$  terms from where multiphonon relaxation can populate  $^2P_{3/2}$  term as observed in [77]. Energy needed for populating these terms is  $> 4.8$  eV which implies that the almost continuous distribution of shallow (usually  $V_0$  type) electron traps up to 0.7 eV below  $ZrO_2$  band-gap can be considered also as excitation centers.

In case of  $^2S_{3/2}$  term and the excited  $^5D_0$  term of  $Eu^{3+}$  the lower energy requirements suggest that the luminous centre can be excited by single mid-gap oxygen vacancy states readily observed also experimentally [29,76]. The broad emission related to the oxygen vacancies is also visible in the luminescence spectrum beneath the  $Er^{3+}$  4f–4f transitions indicating a rather broad range of defect states being present in the crystal. The observed exciton absorption suggests that excitons can also be (at low temperatures) responsible for energy migration to RE ions by trapping at the defect site followed by energy transfer to  $RE^{3+}$ .

## 4.5. Sol-gel prepared $HfO_2$ [paper II]

Sol-gel prepared  $Sm^{3+}$ ,  $Eu^{3+}$  and  $Tb^{3+}$  doped  $HfO_2$  thin films revealed PL specific to the respective  $RE^{3+}$  ions when excited with laser or synchrotron radiation equivalent or higher than band-to-band excitation energy of  $HfO_2$  (see Figure 10).

Compared to earlier studied ALD samples the spectra recorded at 10 K consisted now only of the  $RE^{3+}$  specific transition lines corresponding to the free-ion energy level Stark splitting in crystal field [78,79,80,81]. Rising the temperature to RT broadened the line spectra only slightly. The overall luminescence intensity among the studied dopants was noticeably different. The strongest luminous output was registered for  $Sm^{3+}$  followed by  $Eu^{3+}$  and  $Tb^{3+}$ . The latter is probably affected by different efficiency of the energy transfer mechanism responsible for dopant excitation.

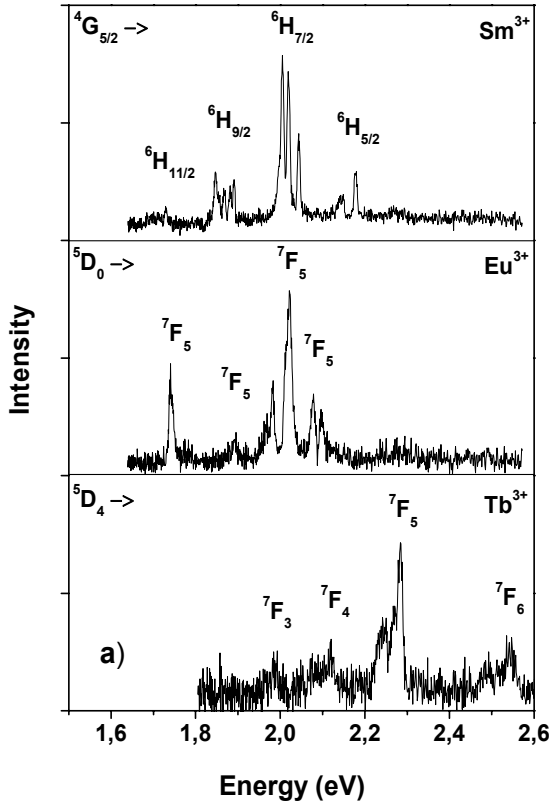


**Figure 10:** PL emission of RE<sup>3+</sup> doped sol-gel prepared HfO<sub>2</sub> under band-to-band excitation at 10K.

samples the exciton absorption is noticeably less pronounced followed by a strong maxima at  $\sim 7.6$  eV. It must be noted that as the spectra are normalized it can be argued that in case of Tb<sup>3+</sup> the exciton absorption is less pronounced because of the higher relative intensity of the 7.6 eV band.

According to Dorenbos [82,83,84,85] a systematic relationship exists between charge transfer band (CTB) energies among rare-earth ions regardless of the host medium. The lowest laying CTB belongs always to the minimal energy needed to lift an electron from ligand valence band to the Eu<sup>3+</sup> ion to form an Eu<sup>2+</sup> ground state. If the absorption of this transition is known the bands for other rare-earth could be predicted. More generally any identified CTB would allow general characterisation of rare-earth ions' ground states positions relative to bands of a particular host. In case of oxides the statistical studies have shown that CTB for Eu<sup>3+</sup> is always at around 4.9–5.6 eV [82,86]. According to the established relationship this gives predicted value for the CTB of Tb<sup>3+</sup> in oxides to be at around 7.5 eV – a good match for the observed value. Regarding the maxima in Tb<sup>3+</sup> doped samples as CTB, the Sm<sup>3+</sup>'s CTB should

As seen from Figure 11 the RE<sup>3+</sup> PL excitation spectra in all three samples were similar in a sense that a sharp onset of excitation was observed at  $\sim 5.7$  eV. Latter is close to the onset of exciton absorption in HfO<sub>2</sub> observed earlier at  $\sim 5.75$  eV. The direct band-gap values were 5.84 eV, 5.71 eV and 6.00 eV for Tb<sup>3+</sup>, Sm<sup>3+</sup> and Eu<sup>3+</sup> doped samples respectively. In among higher energy conduction band states pronounced differences could be noted. Eu<sup>3+</sup> doped sample had a relatively well pronounced exciton absorption band followed by a wider conduction band absorption band peaking around 7–7.5 eV. Same could generally be observed in Sm<sup>3+</sup> doped sample with a bit less clear separation between exciton and conduction band states. In Tb<sup>3+</sup> doped

be at around 6.4 eV. No obvious single identifiable band at that energy can be found. Nevertheless CTB absorption cannot be ruled out as the mixed states of proposed CTB and conduction band states present a somewhat less pronounced separation between exciton and higher energy band absorption compared to  $\text{Eu}^{3+}$  doped sample. In case of  $\text{Eu}^{3+}$  the CTB does not mix with conduction band states making it as a good measure of pure host related excitation with clearly separate exciton absorption maxima.

An important factor to consider is also the relation between the efficiency of host-dopant energy transfer and CTB absorption. As the dopant concentration is not very high CTB could only be observable if the host-related processes are low enough in intensity. Low overall excitation efficiency of  $\text{Tb}^{3+}$  samples via conduction band absorption therefore supports better CTB observability compared to host states. The CTB in  $\text{Sm}^{3+}$  is for the same reason less visible and non-observable relative to host absorption in case of  $\text{Eu}^{3+}$  doped sample.

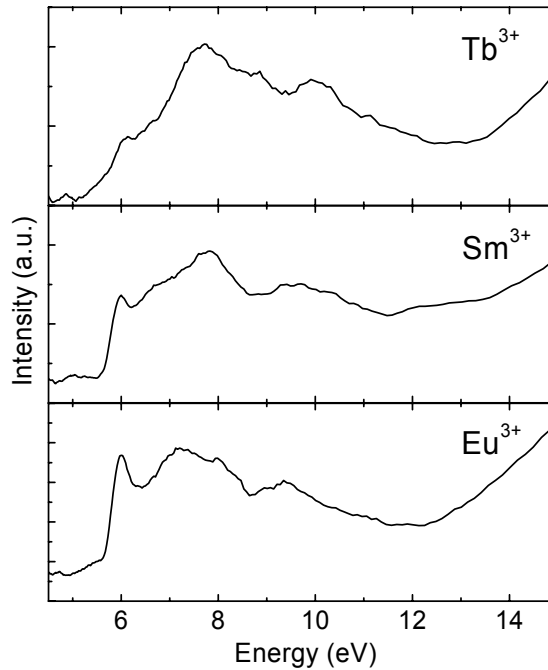


**Figure 11:** Low temperature PL excitation spectra of sol-gel prepared  $\text{HfO}_2$  doped with  $\text{RE}^{3+}$  ions. The excitation is registered for the  $\text{RE}^{3+}$  PL emission.

#### 4.6. Solidification of melt prepared $\text{ZrO}_2$ [paper III]

Bulk samples of solidification of melt prepared  $\text{ZrO}_2\text{:Sm}^{3+}$  had a rather high dopant concentration of 4, 8 and 10 mol% ( $\text{Sm}_2\text{O}_3$ ) respectively. Higher dopant concentration can lead to expected differences in luminescence properties like observability of direct absorption within 4f term energy levels or quenching of luminescence via cross-relaxation. At 405 nm excitation wavelength corresponding to  $^4\text{K}_{11/2}$  term absorption from the  $^6\text{H}_{5/2}$  ground state the samples emitted well resolved Stark split  $\text{Sm}^{3+}$  ion's emission spectra (see Figure 12).

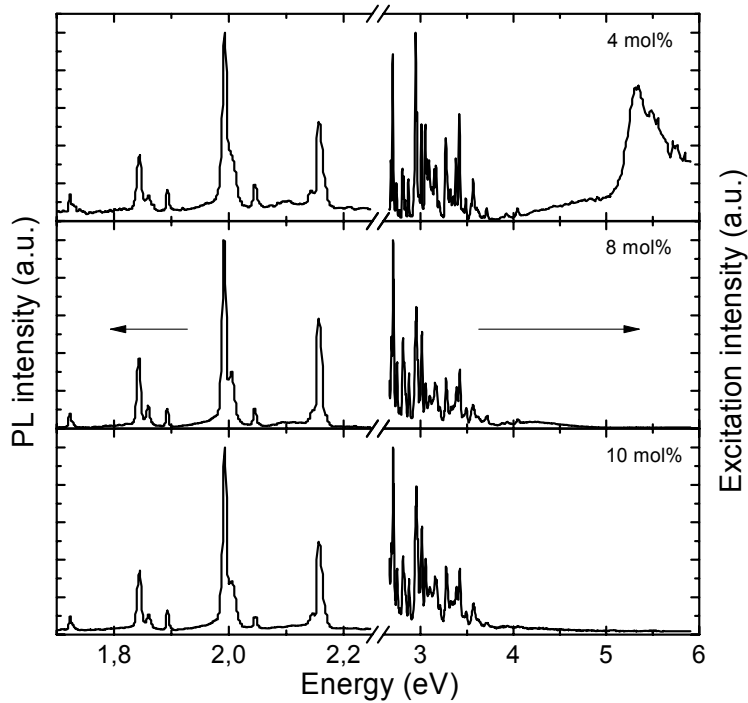


**Figure 12:** Normalised PL (left) and PL excitation (right) spectra of solidification of melt prepared  $\text{ZrO}_2\text{:Sm}^{3+}$  at different doping concentrations.

No intrinsic trapped exciton related emission was detected in higher energy side of the spectrum which could indicate low crystalline quality. The latter is obviously caused by the high oxygen vacancy concentration introduced by dopants.

PL excitation spectra of the  $\text{Sm}^{3+}$  emission (registered at 2.0 eV) corresponding to the strongest  $^4\text{G}_{5/2} - ^6\text{H}_{7/2}$  transition contains numerous sharp 4f direct absorption maxima at energies  $< 4.1$  eV. In the range from 4.1 to 4.9 eV the excitation spectra of 4 mol% doped sample revealed a broad absorption band. This absorption band quenched in intensity as the dopant concentration

was increased to 8 and 10 mol%. Additionally the quenching is dependent on the excitation energy leading to almost complete elimination of excitation above 4.9 eV. In 4 mol% doped sample the quenching is not severe enough and a typical ZrO<sub>2</sub> related excitation spectrum is observed consisting of exciton and conduction band absorption.

Such observations indicate defect related thermal relaxation of the excited charge carriers. At energies exceeding the optical band-gap the relaxation leads to total quenching of the luminescence in case of the 8 and 10 mol% doped samples. This indicates that the excitation energy is relaxed or back-transferred to or between host defect states prior to RE activation. Similar concentration related effect between RE ions has previously been studied in Y<sub>2</sub>O<sub>3</sub> where similar decrease in luminous output starts at ~ 4–5 mol% RE doping [87] or between GaP host crystal and Eu<sup>3+</sup> dopants [88].

## 4.7. Decay analysis

The PL decay of an isolated RE<sup>3+</sup> ion should in ideal case be presented by a ms range single exponent. As demonstrated the excitation and properties of the RE<sup>3+</sup> ions' PL in studied systems relies heavily on the interaction with the host. Therefore the luminescence decay in latter should expectedly be modified to some extent as well.

In Figure 13 the decay of RE 4f–4f luminescence is compared in three ZrO<sub>2</sub> hosts prepared via ALD, sol-gel and skull melting technique. The optically active ion of choice is Tb<sup>3+</sup> in the first case and Sm<sup>3+</sup> in the latter two. Regardless of the inhomogeneous choice of active ion these three samples should reveal the main differences caused by host-dopant interactions and concentration effects in ZrO<sub>2</sub>. Because of similarities the results for HfO<sub>2</sub> are regarded close.

In all three samples the decay of the RE emission (registered at the spectral maxima of <sup>4</sup>G<sub>5/2</sub>–<sup>6</sup>H<sub>7/2</sub> transition in Sm<sup>3+</sup> and <sup>6</sup>D<sub>4</sub>–<sup>7</sup>F<sub>6</sub> transition in Tb<sup>3+</sup>) was not elementary (i.e. not single exponent).

In ALD prepared sample where the dopant concentration was the lowest, two distinct regions could be separated: an almost single exponential decay with decay time of ~860 μs and a long lasting tail (more than few hundred ms in length) starting at > 10 ms.

The observed exponential decay of Tb<sup>3+</sup> is somewhat shorter than reported for free ion in general (1.7 ms) [89,92]. The latter could be attributed to the possible concentration non-homogeneity within the sample. For example the high annealing temperature (1000°C) can cause dopants to migrate to nanocrystallite surface and cause concentration build-up resulting in increased donor-acceptor type cross-relaxation among dopants and leading to shortening of the radiative decay. Comparable decay for Tb<sup>3+</sup> is reported at ~ 1 wt% Tb<sub>2</sub>O<sub>3</sub> doping level in aluminium-silicate glasses [89].



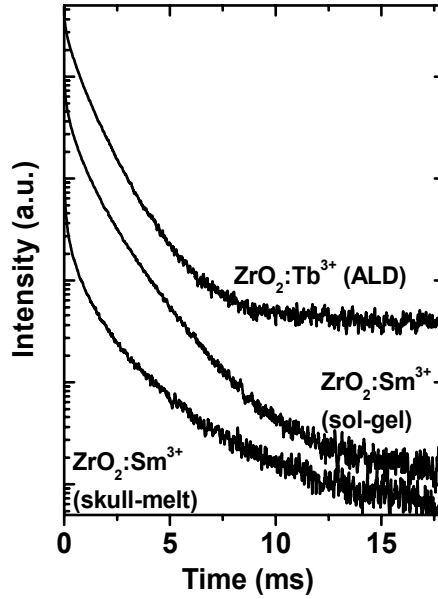


**Figure 13:** PL decay  $\text{RE}^{3+}$  emission in skull-melt (4 mol%  $\text{Sm}^{3+}$ ), sol-gel (0.5 mol%  $\text{Sm}^{3+}$ ) and ALD (0.07 at%  $\text{Tb}^{3+}$ ) prepared samples. The decay profiles are slightly offset for better visibility.

The tail part beyond 10 ms extends further than the detection limit set by laser repetition rate. The best fit for the decay in this region was obtained via  $1/t$  type approximation [93]:

$$I(t) = I_0 (1 + \gamma t)^{-n}$$

This means that the decay follows a power law  $I=f(t^{-n})$ . The fitting value  $n$  was found to be  $\sim 0.46$ .

In literature the  $n$  values around unity are considered as indication of a tunnelling process. In a paper by Yamaga et al. [95] it is concluded that  $n$  much lower than 1 indicates that the trapped hole also “tunnels” to the recombination center by hopping, which requires significant thermal stimulation to overcome the potential barrier between the carrier trap and the destination. As such the tail could in our case be governed by a hopping process where trapped holes or electrons migrate to localised opposite charge at dopant related vacancies. Relatively low overall dopant concentration is the key to observing such a long afterglow.

In sol gel prepared  $\text{ZrO}_2:\text{Sm}^{3+}$  where the dopant concentration is about an order of magnitude higher, no separable time regions were found. Best fit for the whole decay was obtained by stretched exponent approximation with fitting

parameters  $\langle t \rangle = 0.4$  and  $\beta = 0.63$ . The observed non-exponentiality can arise from many different sources. The primary luminescence sites' transition probability could be affected by the local symmetry. Due to inherent need for a charge compensation arising from the substitution of  $\text{Hf}^{4+}$  ions with  $\text{RE}^{3+}$  the sites are usually accompanied by oxygen vacancies. Large number of possible spatial configurations of such  $\text{RE}^{3+} + v$  charge compensator pairs leads to a mixture of site symmetries and consequently to a distribution of decay rates. Charge compensator defects themselves can also lead to efficient de-excitation and thermalisation of the PL sites via non-radiative energy transfer to the latter. The effect is especially pronounced because of spatial proximity to  $\text{RE}^{3+}$ . Due to random nature of defects and energy transfer probabilities to the latter a distribution of shorter decay components is introduced into observable  $\text{RE}^{3+}$  decay.

When the dopant concentration is increased further the stretched exponential decay transforms into time dependence developed by Inokuti and Hirajama [41]. The best fitting was achieved with quadrupole-dipole ( $s=8$  in Eq. 4) interaction model with radiative lifetime of  $\sim 3.5$  ms. This fitting demonstrates substantial donor-acceptor type interaction between more closely packed dopant ions and leads to the observed shortening of the decay compared to true radiative lifetime.

## 4.8. Further discussion

Based on the obtained results few important conclusions can be drawn about the electronic structure and excitation mechanisms in  $\text{RE}^{3+}$  doped zirconium and hafnium oxides.

The optical band-gaps in pure  $\text{ZrO}_2$  and  $\text{HfO}_2$  are at 5.58 eV and 6.15 eV respectively. On the tentative energy level scheme for  $\text{HfO}_2$  (see Figure 14) the gap energy is placed at  $\sim 6.0$  eV to account for the slight reduction seen in sol-gel samples (generally similar scheme applies for  $\text{ZrO}_2$ ).

PL features of pure oxides arise dominantly from trapping sub band-gap exciton or free charge carriers at lattice sites forming self trapped exciton states (in perfect lattice) or defect trapped states (at lattice defects). Relatively high energy recombination emission from these states is in case of  $\text{ZrO}_2$  present only at cryogenic temperatures because of the relatively easy ionization of these states by thermal energy. In  $\text{HfO}_2$  the traps present somewhat deeper states due to wide band-gap resulting in some observable emission even at RT.

The primary source of defects in  $\text{ZrO}_2$  and  $\text{HfO}_2$  are oxygen vacancies. In RE doped crystals where concentration of vacancies is substantially higher, additional optically active defect states form. These deeper trap states spread over relatively wide energy region giving rise to a broad defect related PL emission centered at  $\sim 2.5$  eV. Due to deep mid-gap positioning the emission is also visible at RT.

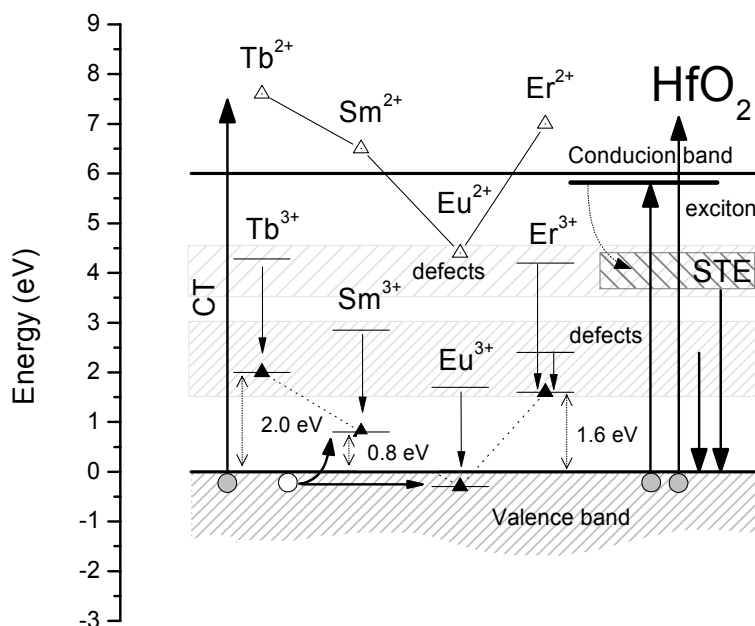


**Figure 14:** Tentative presentation of relative placement of RE<sup>3+</sup> ions 3+ and 2+ energy levels and intrinsic PL states in HfO<sub>2</sub>.

We propose that these states also play substantial role in excitation mechanism of RE<sup>3+</sup> related emission in doped samples as the band represent energetic match to various RE<sup>3+</sup> inter 4f shell transitions allowing non-radiative energy transfer to the latter. Additionally the states can act as thermalisation channels in highly doped (8 and 10 mol%) samples causing emission quenching.

Another important factor in determining indirect excitation efficiency is the energetic placement of the RE<sup>3+</sup> ion 4f energy levels within the host band-gap. The relative placement of RE<sup>3+</sup> ions in respect to host crystal states was established starting from the evidence of CTB absorption in Tb<sup>3+</sup> doped HfO<sub>2</sub>. The CTB absorption at ~ 7.5 eV allowed us to “anchor” Tb<sup>2+</sup> ground state in respect to the valence band of HfO<sub>2</sub>. According to Dorenbos’ empirical observations it was now easy to locate 2+ states of other dopants and somewhat less accurately 3+ ground states.

The placement of the 3+ ground state of Tb ion ~ 2.0 eV above valence band edge renders charge carrier trapping directly from host zones to the ion related states problematic if suitable intermittent states are not present. On the other hand Sm and Eu have their 3+ ground states relatively closer to valence band rendering them better hole traps. Latter increases the excitation efficiency through host related charge carriers and explains the somewhat higher effectiveness of Sm<sup>3+</sup> and Eu<sup>3+</sup> excitation compared to Tb<sup>3+</sup> in HfO<sub>2</sub>.

## **5. $\text{Sm}^{3+}$ AS CRYSTALLOGRAPHIC PROBE IN $\text{ZrO}_2$ [PAPERS III–IV]**

### **5.1. Introduction**

The idea of crystal symmetry sensing via rare-earth ion PL probes is not new. As described earlier the electric dipole transition  $^5\text{D}_0\text{--}^7\text{F}_2$  and magnetic dipole transition  $^5\text{D}_0\text{--}^7\text{F}_1$  of  $\text{Eu}^{3+}$  have successfully been used to probe the site symmetry changes in low symmetry crystal sites [33,34]. Nevertheless despite usefulness the method is almost exclusively restricted to europium ions as no alternative probe with similar sensitivity in visible spectral range is known.

A viable alternative method to the above can be provided by examining the PL fine structure of individual LS terms of rare-earth ions. As known the Stark-Lo Surdo effect causes otherwise degenerated energy terms of rare-earth ions to split in external electric field of the crystal lattice. As a result a fine structure of the optical transitions appears which makes to some extent much of the rare-earth ions suitable for crystal field probing.

Such crystal field effects on rare-earth ions energy terms have been investigated extensively since the early sixties [96]. In a more recent work by De la Rosa et. al. the crystal field splitting of  $\text{Sm}^{3+}$  ion PL has been determined in tetragonal and monoclinic phases of bulk  $\text{ZrO}_2$  [35].

Inspired by the latter experimental results the next paragraphs are dedicated to describe the technical details and results of a partly novel approach of using the  $\text{Sm}^{3+}$  ion as a local symmetry probe for spatial differentiation of crystal phases down to microscopic level in different  $\text{ZrO}_2$  samples.

The developed method uses the virtue of different LS term Stark splitting of the  $\text{Sm}^{3+}$  ion's  $^6\text{H}$  terms in tetragonal and monoclinic crystal surrounding. Different spatial confinements of the excitation of  $\text{Sm}^{3+}$  ions will be achieved by the use of confocal microscopy, micro-mapping and different excitation energies.

Such approach is superior to conventional XRD and Raman measurements because of its spatial selectivity and higher efficiency. Compared to Raman the excitation cross-section of PL is  $\sim 10^4$  times higher allowing much smaller amounts of material to be characterized. As such the PL based detection method could in theory be used even at nano scale when single atom emitters and fluorescence resonant energy transfer (FRET) microscopy is used [97].

### **5.2. Experimental setup**

Detecting the spatial distribution or segregation of different crystallographic phases is informative only when mixed phase content exists. According to established dopant stabilised phase equilibrium in  $\text{ZrO}_2$  (see Chapter 2.5) it can be assumed that high doping ( $> 1 \text{ mol}\%$ ) can in many cases result in phase

mixtures being present at room temperature. Skull-melt prepared samples are therefore especially interesting as their  $\text{Sm}^{3+}$  content was as high as 4, 8 or 10 mol% and according to XRD studies contained phase mixtures at 4 and 10 mol% doping concentration.

For resolving the spatial phase distribution within those samples a spatially resolved mapping of PL signal (and Raman signal for comparison) was carried out using Renishaw confocal micro-Raman setup. The microstage and confocal optical setup of the microscope permitted Raman and PL signal gathering from spot size down to  $\sim 1\mu\text{m}$ . In each spot the spectrum was collected in special step scanning mode where both the Raman signal from  $\text{ZrO}_2$  lattice as well as PL of  $\text{Sm}^{3+}$  were covered simultaneously in one scan of the spectrograph (from 488–750 nm). For both Raman and PL measurements 488 nm  $\text{Ar}^+$  laser excitation was used. The microscope was fitted with a 50x glass objective. The registration of spectra was done by integrated grading spectrograph fitted with CCD camera and mathematically processed to produce maps of PL as well as Raman signal intensities over scanned surfaces. As the scattering properties of the samples didn't allow three dimensional scanning the main results are obtained by mapping different macroscopic surfaces of the samples.

Additional spatially integrated PL measurements were carried out on the already introduced back scattering PL measurement setup (see Paragraph 4.2) with the aid of OPO and xenon lamp excitation sources. For reliably determining all different phase surroundings for the emitting ions a combined emission excitation spectra (CEES) was measured. In the first stage numerous PL spectra were registered with OPO excitation. Afterward the xenon lamp excitation was used to measure the continuous excitation spectra for one of the  $\text{Sm}^{3+}$  ion PL transitions to calibrate the intensities of OPO spectra. Finally a computerised extrapolation was done to ensure continuous data in both excitation and emission datasets.

## 5.3. Results

### 5.3.1. Raman measurements

Initial characterization of the phase content of the materials was done via Raman measurements on randomly selected spots over the samples. According to the results (see Figure 15) the 8 mol% Sm doped  $\text{ZrO}_2$  was the purest in composition. Because of the well established 6 Raman active modes ( $A_{1g}+2B_{1g}+3E_g$ ) of tetragonal symmetry (phase group  $D_{4h}$ ) full tetragonal structure was assumed. In 10 mol% doped sample the tetragonal modes are suppressed by about two times accompanied most prominently by the cubic fluoride type high symmetry  $T_{2g}$  mode at  $610\text{--}620\text{ cm}^{-1}$  [90,91]. The latter is overlapping with tetragonal modes which means only slight broadening of the mode is observable in addition to the intensity increase. The phase structure in

the latter sample is considered as mixture of cubic and tetragonal phases. From XRD measurements it had been estimated that the t/c phase ratio in the sample was similarly close to unity [64].

In 4 mol% doped sample the tetragonal modes are also somewhat lower in intensity accompanied with additionally signs of some of the 18 ( $9A_g + 9B_g$ ) theoretically predicted low symmetry modes of monoclinic structure [98] (see Figure 15).

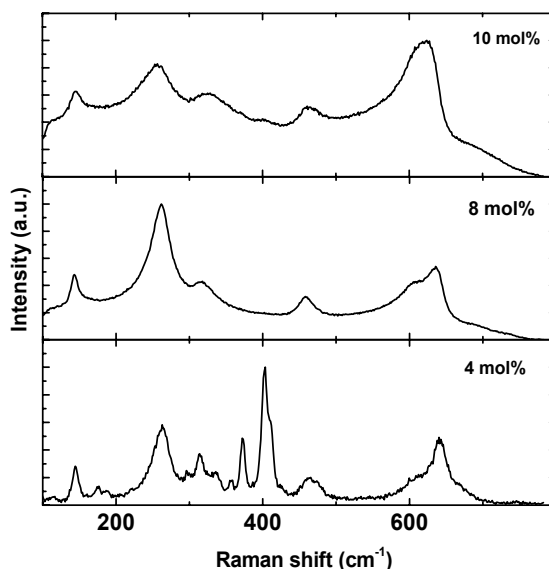


**Figure 15:** Raman spectra of zirconia samples doped with different molar ratio of  $Sm^{3+}$  ions.

For determining the best spot for phase mapping next the samples were measured from several random locations. The results for 8 and 10 mol% doped samples remained the same all over the macroscopic surfaces whereas in 4 mol% doped sample significant change in Raman signal was found when the sample was measured from a  $90^\circ$  angle to the initial plane. The new surface presented substantial rise in monoclinic phase content among tetragonal. Additionally the relative intensity of the modes became dependent on the lateral location on the sample (see Figure 16).<sup>1</sup>

<sup>1</sup> The photoluminescence line at  $403\text{ cm}^{-1}$  denoted as PL on figure was identified most likely as PL from samarium  $^4I_{9/2}$  level to ground state  $^6H_{5/2}$  [94].

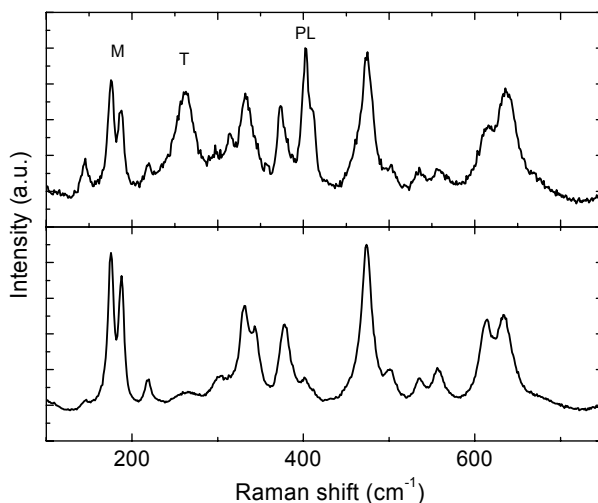


**Figure 16:** Raman spectra from different regions of the zirconia crystal. T, M and PL indicate the characteristic lines for tetragonal, monoclinic and photoluminescence.

The relative content of monoclinic and tetragonal phases on the new surface was estimated according to Garvie and Nicolholson's empirical equation [99]:

$$C_m = \frac{I_m^{179} + I_m^{190}}{I_T^{264} + I_m^{179} + I_m^{190}} \quad \text{Eq. 11}$$

Here the different terms denote integral intensities of the Raman lines at indicated Raman wavenumbers. According to Eq. 11 the Raman signal (Figure 16) suggests that the phase-mixed sample has different surroundings present ranging from mixture of tetragonal ( $C_t=52\%$ ) and monoclinic ( $C_m=48\%$ ) phases to a lesser amount of almost totally monoclinic regions ( $C_m=98.6\%$ ).

### 5.3.2. CEES measurements

In order to detect all possible phase regions within the sample CEES spectrum was next registered (see Figure 17).<sup>2</sup>

---

<sup>2</sup> Spectra are characterised by their wavelengths rather than energy (used earlier) from this point onwards as more commonly used unit for characterising RE ions spectroscopic properties.

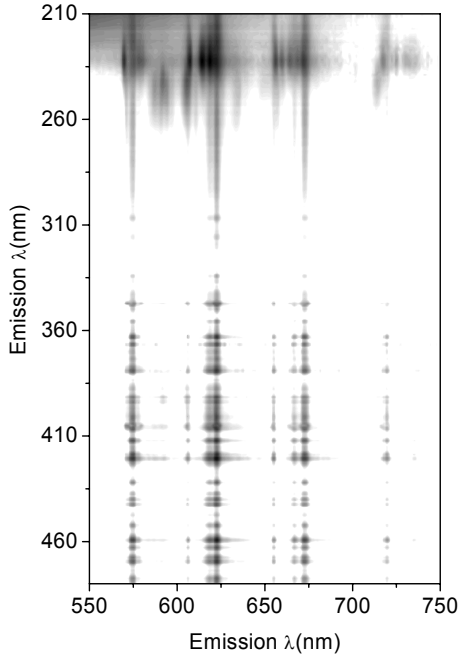


**Figure 17:** The combined excitation-emission spectra of Sm-doped ZrO<sub>2</sub> measured at 6 K. For coverage of the whole range of emission intensities a logarithmic scale is used.

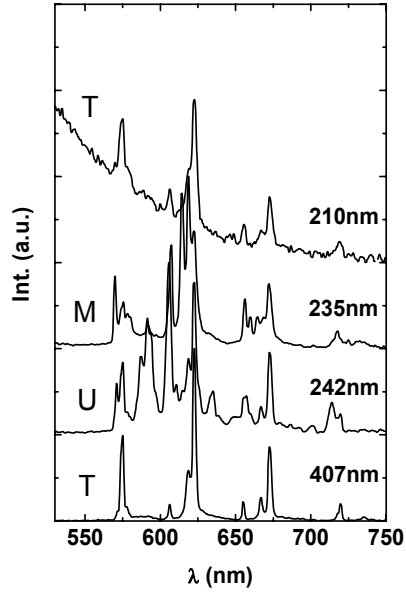


**Figure 18:** Low temperature (6K) Sm<sup>3+</sup> emission spectra at tetragonal (T), monoclinic (M) and unknown (U) sites of ZrO<sub>2</sub> at different excitation wavelengths. Measured at 6 K. (Spectra are shifted for clarity in intensity scale.)

Compared to Raman measurements PL emission's CEES study can better reveal the phase composition of the sample as PL emission's excitation quantum efficiency is higher and the added virtue of charge carrier mobility at excitation energies close to and exceeding host band-gap could reveal sites otherwise spatially non-reachable or too low in concentration.

In CEES spectra measured from 4 mol% doped sample (see Figure 17 and Figure 18) two distinct regions of Sm<sup>3+</sup> excitation are revealed. At excitation wavelengths from 470 to ~300 nm the directly excited highly fluctuating (depending on excitation wavelength) PL emission characteristic to 4f–4f transitions of Sm<sup>3+</sup> ions was present. Below 300 nm the spectra represent a more uniform excitation region of zirconia host related absorption.

By comparing PL spectra derived from CEES spectrum with the previous results for the Stark splitting of the <sup>4</sup>G<sub>5/2</sub> to <sup>6</sup>H<sub>i</sub> (i = 11/2, 9/2, 7/2 and 5/2) term emission of Sm<sup>3+</sup> ion in tetragonal and monoclinic crystals [35,100] we can suggest that in current case Sm<sup>3+</sup> ions both in the tetragonal and monoclinic crystal sites are indeed present at excitation wavelengths 407 and 235 nm respectively (see Figure 18). Additionally a third, lower symmetry (denoted as



“unknown”) crystalline surrounding is presented by the additional PL lines at excitation wavelength of 242 nm.

In 8 and 10 mol% doped samples the only visible emission originated from tetragonal phase. At higher energies small evidence of the low symmetry “unknown” phase region was also detected but with greatly reduced intensity. No emission from pure monoclinic phase was detected.

The excitation spectra (see Figure 19) derived from the CEES spectrum for the most characteristic Stark components of each phase revealed noticeable differences. Tetragonal phase is excited with varying intensity over the whole measured excitation wavelengths range from 210 to 480 nm (for UV part see Figure 19). The excitation follows well the known exciton and conduction band absorption ( $\lambda_{\text{ex}} < 235$  nm) with a noticeable tail extending from 235 to ~300 nm. Similar band at around 300 nm has previously been seen and attributed to host absorption in  $\text{ZrO}_2$  [101]. Monoclinic sites are excited prevalently in noticeably smaller band centered at ~235 nm correlating most notably with the exciton absorption with reduced efficiency from conduction band states. The low symmetry phase is excited in as small band centered at ~240 nm (see Figure 19a). The latter maximum shifts to 250 nm at RT (see Figure 19b) with additional absorption appearing at exciton absorption peak.

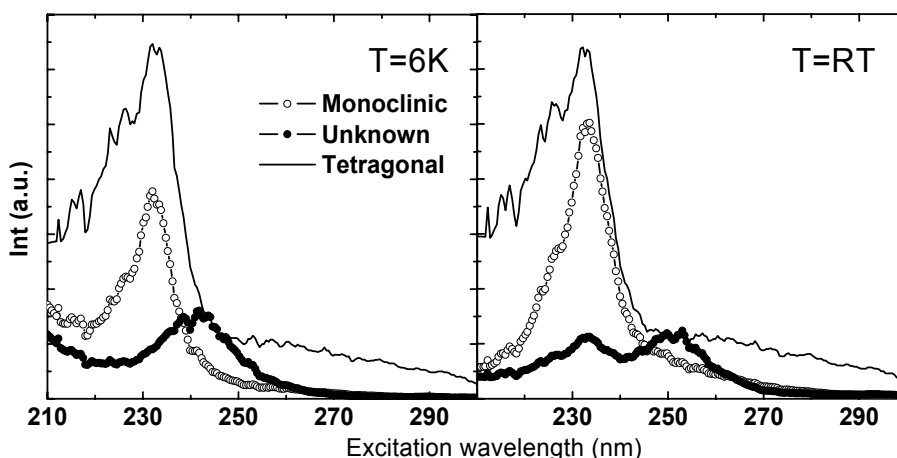


**Figure 19:** Excitation spectra of the  $\text{Sm}^{3+}$  emission in tetragonal, monoclinic and unknown phases of  $\text{ZrO}_2$  at 6 K and RT.

### 5.3.3. PL decay measurements

The emission decay (see Figure 20) measured at the highest intensity tetragonal transition line at 623 nm is evidently nonexponential. The emission from the monoclinic transition line at 607 nm reveals a strongly nonexponential retarded decay extending to several hundred milliseconds. Emission decay from the

unknown phase sites was almost exponential at 6K but reduced into unresolved shorter non-exponential process at RT (see Figure 20).

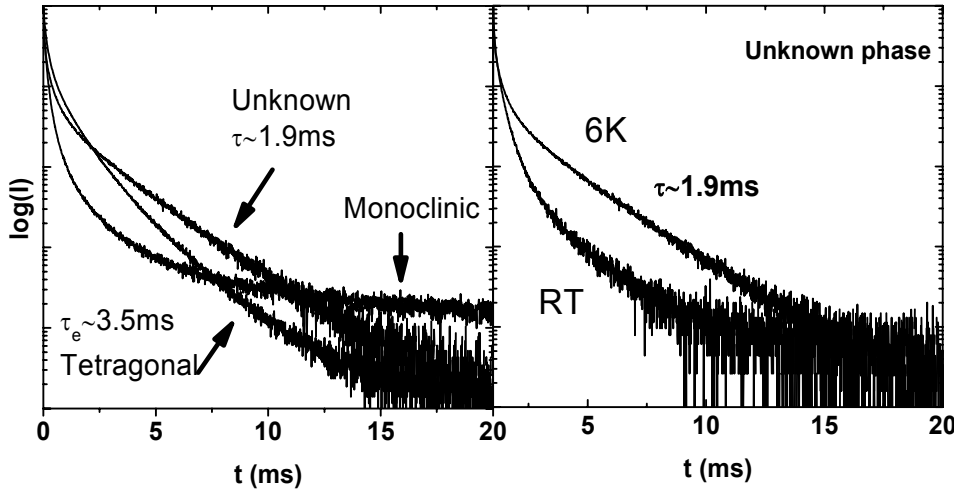


**Figure 20:** PL decay curves of  $\text{Sm}^{3+}$  ion emission in different surroundings of  $\text{ZrO}_2$  matrix, measured at 6 K (left); temperature dependence of the PL decay of the  $\text{Sm}^{3+}$  ion in the unknown site of  $\text{ZrO}_2$  (right).

#### 5.3.4. Excitation mechanisms

The different surroundings evidently cause three different routes of excitation for  $\text{Sm}^{3+}$  ions. In tetragonal sites where  $\text{Sm}^{3+}$  ions are prominently excited via direct absorption ( $\lambda_{\text{ex}} > 300 \text{ nm}$ ) the decay is non-exponential and best described by the empirical model proposed by Inokuti and Hirajama [41] (see Chapter 4.7). This inherently means that the PL is influenced by high concentration and no long range migration of excitation is expected.

The monoclinic sites are excited primarily through exciton absorption band at 235 nm. The retarded decay is indicating that a tunnelling processes similar to the one observed in ALD prepared  $\text{HfO}_2$  (see Chapter 4.7) could govern the recombination process. Long migration means that the charge carriers (most probably electrons) are able to move considerably before trapping. Once trapped by localised holes' Coulomb field within close distance from  $\text{Sm}^{3+}$  ion the non-radiative energy transfer occurs.

The unknown phase where remaining emitting  $\text{Sm}^{3+}$  ions are located is presumed to reside on the interface of monoclinic and tetragonal phase or on the nanocrystallite surfaces as the symmetry of the sites tend to be even lower than that of the monoclinic sites (more Stark components). The low temperature almost exponential decay of the luminescence indicates that the sites are deeply

localised. At RT thermally induced relaxation processes cause the decay to become non-exponential and shortened and also lead to the appearance of the excitation peak at exciton absorption wavelength. It can be suggested that it could be an indication that a donor level from the monoclinic phase has been opened for  $\text{Sm}^{3+}$  ion excitation via temperature assisted multi-phonon relaxation. The latter can lead to energy migration from initially highly mobile charge carriers in monoclinic phase to the interface layer.

### 5.3.5. Spatial mapping

In order to resolve the actual spatial distribution of the monoclinic and tetragonal phases within the 4 mol% doped sample next a detailed mapping of Raman as well as PL signal was carried out on the  $90^\circ$  angle surface.

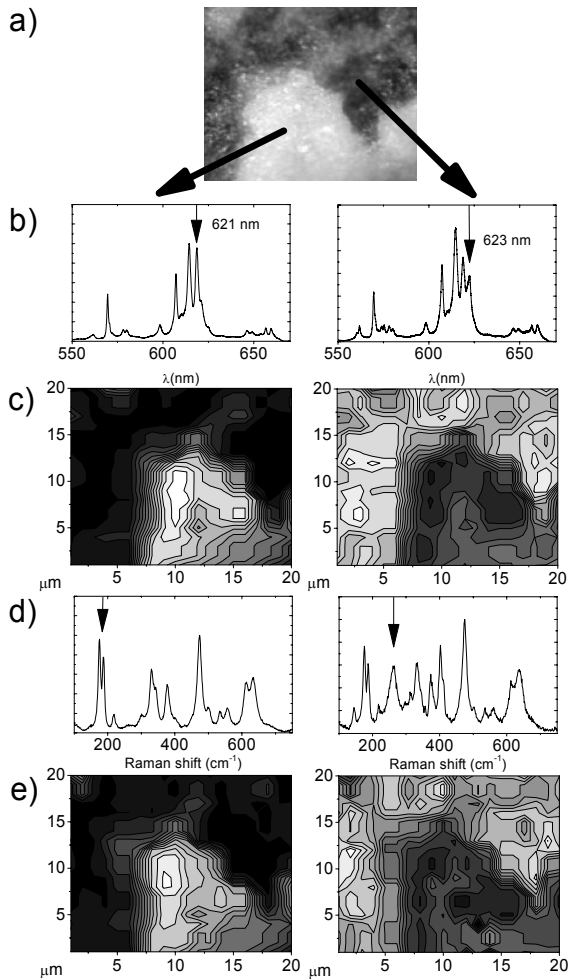


**Figure 21:** Spatial segregation of monoclinic and tetragonal phases of 4 mol% Sm-doped  $\text{ZrO}_2$  revealed by micromapping of sample: a – visible image; b –  $\text{Sm}^{3+}$  spectra of different areas of sample, c – spatial location of monoclinic and tetragonal phases revealed from the fine structure of  $\text{Sm}^{3+}$  emission; d – Raman spectra of different areas of sample; e – location of M and T phases revealed from the Raman spectra.

On the optical visible light micrograph two distinct regions can be differentiated (see Figure 21a). The darker and lighter areas are assumed to be caused by different light scattering properties of monoclinic and tetragonal  $\text{ZrO}_2$  respectively. Such difference can arise due to inherent un-match between the nanocrystallite sizes in tetragonal and monoclinic crystal leading to unavoidable break up and defect generation in the area occupied by different (larger) unit cell monoclinic nanocrystallites placed within tetragonal surrounding.

The laser wavelength used (488 nm) in the experiment suggests that primarily tetragonal phase sites should be excited upon photoexcitation as observed in CEES spectra earlier. Despite that the PL spectra of the  $\text{Sm}^{3+}$  was more or less monoclinic in both regions. As can be seen on Figure 21b the characteristic tetragonal phase luminescence line at 622 nm was still present but only barely pronounced compared to monoclinic lines in the same multiplet. When the relative fluctuations of the 622 nm line was compared to that of the other lines in the multiplet a clear correlation with the optical micrographs was revealed on Figure 21c.

Comparative study was carried out on characteristic Raman resonances (indicated on Figure 21d with arrows) for monoclinic and tetragonal phases respectively (see Figure 21e). Latter confirmed the correlation. Despite the strong presence of monoclinic phase in both areas tetragonal phase was in anticorrelation with the former and more pronounced in darker areas on the micrograph.

### **5.3.6. Proposed model for phase segregation**

Latter results can be used to postulate tentative model of the spatial phase mixing within the sample.

When the sample is viewed in plane of the originally studied (diamond cut) surface a set of three different sites can be excited out of which monoclinic and the “unknown” interface phase can be excited only through mobile charge carriers of the host. This indicates that the majority volume of the material exposed to the experiment is macroscopically tetragonal. On the contrary when the sample is studied from 90° degree angle, monoclinic phase is prevailing regardless of the area examined. This indicates that the monoclinic phase is arranged in thin layers perpendicular to the first surface and only detectable directly from angled view (see Figure 22).

The high defectiveness of the monoclinic layer leads to a situation where the laser excitation in angled view primarily excites monoclinic phase PL as the direct absorption as well as scattering in tetragonal regions is low.

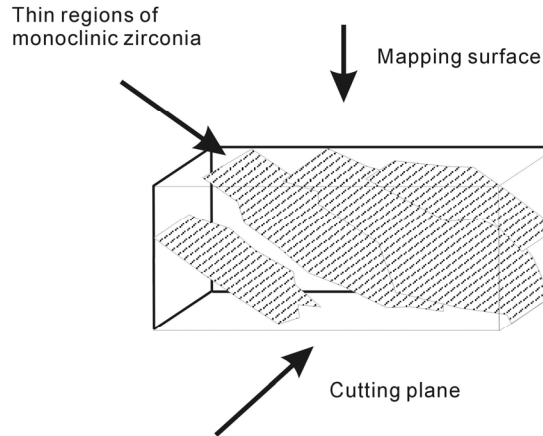


**Figure 22:** A scheme of the proposed orientation of monoclinic phase segregation areas inside the 4 mol%  $\text{Sm}^{3+}$  doped  $\text{ZrO}_2$ .

Phase segregation even thou not very similar has been seen also in  $\text{Al}_2\text{O}_3$  doped  $\text{ZrO}_2$  by Yu. Pudalov et. al. [102]. In observed segregation the separate regions were proposed to have been formed by  $\text{Al}_2\text{O}_3$ - $\text{ZrO}_2$  associates that have higher melting temperature and higher coordination number compared to pure  $\text{ZrO}_2$  melt. The two types of melt remained incompatible and spatially separated also after cooling down.

## **6. PHASE STABILIZATION OF SOL-GEL MICROROLLS [PAPER V]**

### **6.1. Introduction**

Sol-gel microrolls are novel microstructures containing rolled up less than a micrometer thick layers of oxide material. Such structures have rather large surface area and contain empty space in around their axis. Such properties can arguably lead to many different applications like: improved gas sensors, vessels for controlled release of medicines, waste water filters etc.

As the microstructure of the material is rather important in defining its properties precise control of its growth method is highly important. It can be expected that apart from the wet-chemical preparation route described for  $\text{ZrO}_2$  based microrolls in Chapter 3.3 the thermal treatment often used for forming crystalline structure can cause substantial changes in the formed rolls. The main driver for the latter is the temperature assisted phase changes that could change the size and even destroy the delicate structure.

The promising results from the phase mapping experiments of  $\text{ZrO}_2$  samples from the last chapter suggest that the PL emission of the  $\text{Sm}^{3+}$  ion could indeed be used for estimating the phase content in  $\text{ZrO}_2$ . Furthermore it was shown that if the properties of excitation and charge carrier mobility are known the PL emission can be used for estimating rather complex segregation patterns.

In the following experimental work this idea is further developed to achieve spatial confinement of the PL probes via controlling the excitation penetration depth in  $\text{Sm}^{3+}$  doped zirconia. In conjunction with Raman and XRD measurements a detailed picture of the phase composition and its temperature dependence are given. The result will help to understand better the difficulties caused by phase changes in zirconia microrolls caused by heat treatment.

### **6.2. Experimental setup**

During the experiment the  $\text{Sm}^{3+}$  doped  $\text{ZrO}_2$  microrolls were annealed in subsequent steps from 500 to 800°C in steps of 100°C. Next the phase content as well as its placement within the rolls was characterized in all samples by PL, Raman and XRD measurements. The PL excitation at 405, 250, 235 and 210 nm was carried out with OPO and by a solid state diode-pumped laser operating at 473 nm. For Raman measurements the already described Renishaw micro-Raman microscope was used with 488 nm laser excitation. The XRD patterns of each sample were recorded on a Bragg-Brentano diffractometer “DRON-3M” using  $\text{CuK}\alpha$  radiation in step scanning mode from 15° to 70° at 0.02° increasements of 2 $\theta$  at 5 seconds per step. Weight fractions (mass%) of the tetragonal and monoclinic phases were determined by Rietveld refinement using

program FULLPROF. Visible micrographs were recorded with imaging CCD mounted on a Olympus optical microscope fitted with 20x magnification objective. The scattering SEM images were acquired by Tescan Vega electron microscope.

### 6.3. Results and discussion

The bulk excitation of the samples under 473 nm laser excitation revealed that there exists a clear boundary condition for annealing temperature beyond which the  $\text{Sm}^{3+}$  ion's luminescence can effectively be excited. The as prepared microrolls revealed almost no detectable luminescence up to annealing temperature of 700°C after which however strong  $\text{Sm}^{3+}$  emission with Stark components characteristic to monoclinic crystal phase emerged (see Figure 23). According to XRD studies the phase composition of the samples was almost completely tetragonal at 500 to 600°C and turned promptly monoclinic after annealing at 700°C (see Figure 24).

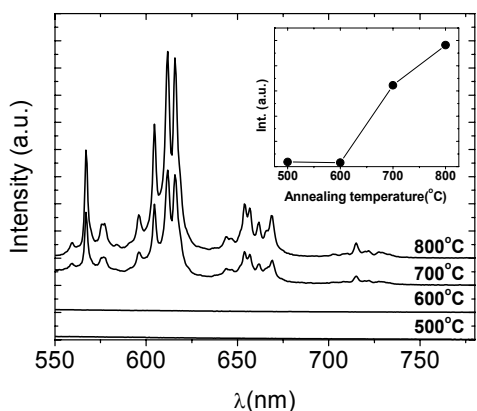


**Figure 23:** Development of  $\text{Sm}^{3+}$  PL emission during annealing cycle from 500°C to 800°C under direct photo-excitation at 473 nm. Insert: the increase of integral intensity of emission (spectra are intensity shifted for clarity).

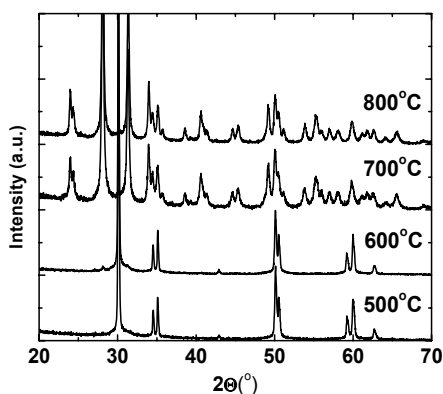


**Figure 24:** XRD spectra of the microrolls after annealing at different temperatures (spectra are intensity shifted for clarity).

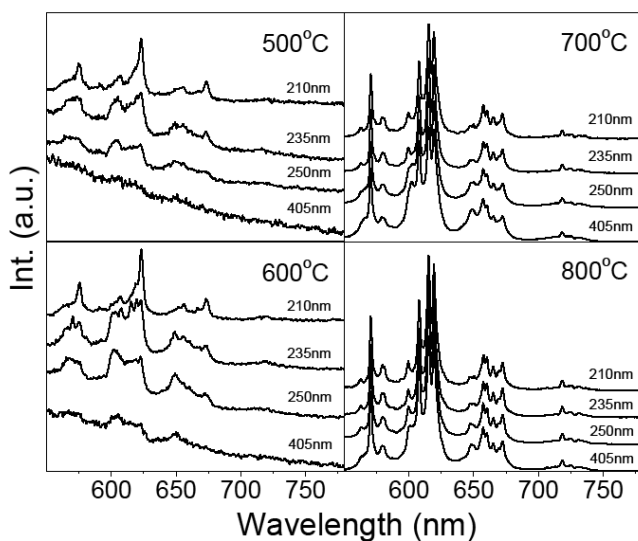


**Figure 25:** Normalised PL of  $\text{Sm}^{3+}$  ions excited at different wavelengths in  $\text{ZrO}_2$  microrolls annealed in cycle from 500°C to 800°C.

Regardless of the low excitation efficiency below 700°C next an attempt was made to investigate the confinement of the different crystallographic phases within the rolls at each annealing temperature. For that PL excitation measurements of the  $\text{Sm}^{3+}$  luminescence were carried out at wavelengths with vastly different absorption depths in the  $\text{ZrO}_2$  host allowing monitoring the phase composition separately on the surface and inside the zirconia nanocrystallites.

According to the results (see Figure 25) any excitation less in energy than the principal band-gap of zirconia ( $\sim 210$  nm) resulted in poorly resolved weak  $\text{Sm}^{3+}$  PL emission in below 700°C annealed samples. At 210 nm the emission is somewhat higher in intensity and indicates the presence of tetragonal surrounding for the emitting ions. In samples annealed at above 700°C the PL emission is orders of magnitude higher in intensity and according to the spectral features is composed of monoclinic phase regardless of the excitation wavelength.

The apparently low excitation efficiency of the mainly tetragonal phase samples (500°C and 600°C annealed) could be explained by a fact that the sol-gel technique leaves substantial amount of organic molecules into the formed microrolls that do form vacancies and other types of defect-centers. The latter are also responsible for the broad band emission (see Figure 25) in accordance with [103]. These additional undesired dopants and related defects account for roughly 4% of the total mass of the samples according to Rietveld analysis and therefore can play substantial role in quenching the  $\text{Sm}^{3+}$  emission. Alternatively clustering of  $\text{Sm}^{3+}$  ions can be considered which raises the probability



of cross-relaxation. At the very surface of the crystallites the concentration of defects is lower due to annealing thus allowing the  $\text{Sm}^{3+}$  emission to strengthen.

From the observations it is evident that in the microrolls undergo an almost complete transformation from tetragonal to monoclinic phase at annealing temperature of 700°C.

The fast phase transformation can be explained by considering the macroscopic shape of the rolls. In general the  $\text{Sm}^{3+}$  concentration in the rolls was too low (0.5 mol%) to stabilise the tetragonal phase alone. Therefore at least some other factors should be taken into account. The most probable are the size effect, the shear stress caused by rolling up the material and the effect of organic matter left from the sol-gel solvent. By considering the Gibbs free energy model described in chapter 2.5 the contribution from the latter factors is rather difficult to quantitatively characterise. Nevertheless a qualitative model can be proposed. In general the transition to monoclinic phase happens when the potential barriers of relevant factors in Gibbs free energy equation are lowered enough for the net energy change to be negative value (i.e. towards a lower energetic state). As shear stresses are integral part of the rolled material and do not change the transition to monoclinic phase happens when either the concentration of organic dopants decreases due to annealing, lowering the overall stresses applied to forming crystallites, and/or the average size of the tetragonal crystal exceeds a threshold value where the surface free energy change ( $\Delta S$ ) is low enough to for the transition to happen. As the tetragonal crystallites grew this net effect must have overcome the surface energy change barrier at 700°C leading to the rapid transformation to monoclinic phase. Because of the unit cell size difference the transformation also lead to twin boundary creation as smaller monoclinic crystallites formed.

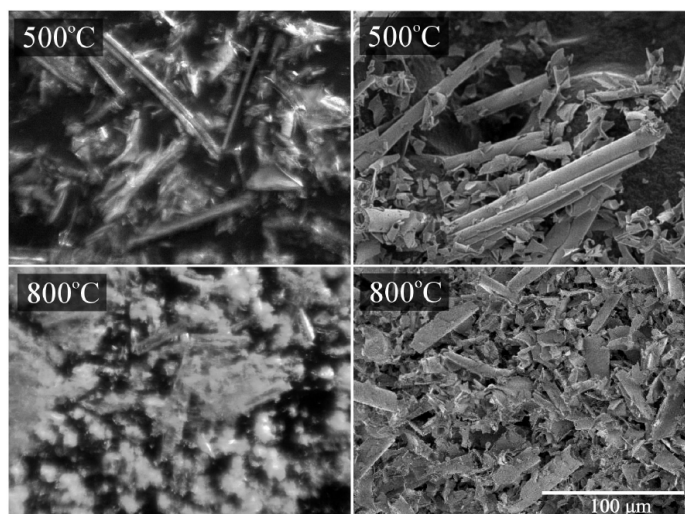


**Figure 26:** Optical micrographs (left) and corresponding SEM images (right) of the microrolls at different annealing temperatures.

According to the average broadening of the FWHM in XRD reflection maximas from  $0.13^\circ$  to  $0.26^\circ$  from tetragonal to monoclinic samples it is estimated that the monoclinic phase nanocrystallites are on average 2 or more times smaller than that of the tetragonal nanocrystallites. The latter inevitably proves the creation of twin crystallites and is the cause for the production of large amount of cracks [104]. Latter can be observed on the optical micrographs and corresponding SEM images on Figure 26. It is clearly seen that the microrolls have lost a bit of their initial diameter and on average shortened in length during the annealing cycle.

## 6.4. Conclusion

Based on the study conducted on the sol-gel prepared  $\text{ZrO}_2$  microrolls several problems concerning the preparation or the rolls as well as the PL based phase detection method are revealed.

Despite the high excitation efficiency compared to Raman scattering the PL based method is highly influenced by the surrounding crystal structure and can in extreme cases be almost useless if good energy back-transfer mechanisms between the probe and host crystal exist that can thermalise the PL emission.

Secondly it must be noted that in preparation of the sol-gel microrolls the phase changes can lead to almost complete destruction of the microstructures. For practical use a fine balance must be found between the accepted level of low quality crystal structure and the destruction of the microstructures themselves.

## SUMMARY

The present work has been devoted to the study of the spectroscopic properties and phase-change dynamics of pure and rare earth doped  $\text{ZrO}_2$  and  $\text{HfO}_2$ . The performed experimental and theoretical work included: preparation of samples; XRD, spectroscopic, and Raman measurements; ab initio modelling of the structural, electronic and optical properties of the prepared samples; and interpretation and analysis of the obtained results.

In the first part of the work extensive investigation of intrinsic as well as RE dopant related PL processes was conducted via spectroscopic means.

The main conclusions of the performed research can be summarized as follows:

1. Efficient energy transfer from host generated charge carriers to RE ions has been shown to take place via charge transfer or various oxygen vacancy related localised states.
2. The relative placement of various RE ions' ground state energy levels within  $\text{ZrO}_2$  and  $\text{HfO}_2$  band-gap have been estimated.
3. Depending on dopant concentration charge carrier tunnelling, oxygen vacancy trapping and inter ionic relaxation have been shown to govern the PL relaxation processes of  $\text{RE}^{3+}$  photoluminescence in  $\text{ZrO}_2$  and  $\text{HfO}_2$ .
4. The introduction of oxygen vacancies (intrinsic or dopant related) is shown to cause reduction in  $\text{ZrO}_2$  and  $\text{HfO}_2$  conduction band width from  $\sim 10$  eV down to 2–3 eV.

Second part of the thesis was investigating the possibility of using novel  $\text{Sm}^{3+}$  dopant luminescence based method for crystal phase detection within  $\text{ZrO}_2$ . General aim was to study both the usefulness of the method and to resolve the phase content as well as its growth dynamics in  $\text{ZrO}_2$ . The result of the study can be summarized as follows:

5. A novel crystal phase detection method based on different Stark splitting patterns of  $\text{Sm}^{3+}$  ion LS terms photoluminescence has been introduced. Defect related non-radiative relaxation channels of sol-gel prepared  $\text{ZrO}_2$  have been shown to limit the use of the method by effectively reducing the luminous output.
6. Micro scale phase segregation of monoclinic and tetragonal phases in skull-melted  $\text{Sm}^{3+}$  doped  $\text{ZrO}_2$  has been spatially resolved revealing a peculiar microscale layered distribution of tetragonal and monoclinic phases.
7. PL emission based phase detection method has been used for monitoring the growth and confinement properties of tetragonal crystal phase in  $\text{ZrO}_2$  microrolls. Its rapid transformation to monoclinic at  $700^\circ\text{C}$  has been determined to lead to the destruction of the microroll structure.

## SUMMARY IN ESTONIAN

Töö pealkiri: “Harulaste muldmetallidega dopeeritud ja dopeerimata  $\text{ZrO}_2$  ja  $\text{HfO}_2$  spektrsoskoopilised ja faasi-stabilisatsiooni omadused”

Käesolev töö on pühendatud spektroskoopiliste- ja faasidünaamika omaduste uurimisele puhtas ja haruldaste muldmetallidega dopeeritud  $\text{ZrO}_2$ -s ja  $\text{HfO}_2$ -s. Läbiviidud eksperimentaalne ja teoreetiline töö hõlmas endas: katseobjektide valmistamist; röntgenhajumist, spektroskoopilisi ja Raman uuringuid; struktuursete, optiliste ja elektrooniliste omaduste teoreetilist arvutamist ja tulemuste sügavamat analüüsi.

Töö esimeses osas vaadeldi täpsemalt  $\text{ZrO}_2$  ja  $\text{HfO}_2$  s toimuvaid omakiirgus ja haruldaste muldmetallidega seotud kiirgusprotsesse kasutades spektroskoopia vahendeid. Uurimistöö tulemusena on saadud järgmised tulemused:

1. On näidatud efektiivse energia ülekande toimumist oksiidi ja muldmetallilisandite vahel nii laengu ülekande kui oksiidmaterjalis esinevate hapniku vakantsidega seotud defektiseisundite kaudu.
2. On hinnatud mitmete haruldaste muldmetallide energiatasemete suhtelist paiknemist  $\text{ZrO}_2$  ja  $\text{HfO}_2$  keelutsoonides.
3. On näidatud muldmetallilisandi luminesentsi kustumiskineetika sõltuvust tema konsentratsioonist. Viimane on domineerivalt kas laengukandja tunneleeriumise, hapniku vakantsidel lõksustumise või ionide vahelise interaktsiooni poolt mõjutatud
4. On näidatud, et hapnikuvakantside lisamine kristallvõre koosseisu vähendab uuritud oksiidides juhtivustsooni laiust  $\sim 10$  eV-lt 2–3 eV-ni.

Töö teises osas vaadeldi lähemalt  $\text{Sm}^{3+}$ iooni kasutuse võimalikkust kristalli struktuuri detektorina. Eesmärgiks seati nii meetodi kasutuskõlblikkuse analüüs kui ka reaalsete faasikoostiste määramine nii tsoon-sulatus kui ka sool-geel meetodil valmistatud  $\text{ZrO}_2$  objektides. Saadud tulemused on järgmised:

5. On juurutatud uudne  $\text{Sm}^{3+}$ iooni luminesentsi Starki komponentide lõhenemise erinevustel põhinev kristalli faasi detekteerimise meetod. On leitud, et viimase kasutamist võivad takistavad peamiselt defektidest tingitud mittekiirguslikud relaksatsioonikanalid.
6. On tuvastatud eriline kihiline monokliinse ja tetragonaalse faasi segregatsioon  $\text{Sm}^{3+}$ -ga dopeeritud  $\text{ZrO}_2$ -s.
7. Väljatöötatud spektroskoopilist meetodit kasutades on jälgitud kristallse faasi kasvamist ja ruumilist paiknemist sool-geel mikrorullides. On leitud, et viimastes  $700^\circ\text{C}$  juures toimuv faasisiire teragonaalsest monokliinsest põhjustab mikrostruktuuride ulatuslikku purunemist.

## REFERENCES

- 1 K. W. Krämer, P. Dorenbos, H. U. Güdela and C. W. E. van Eijk, *Journal of Materials Chemistry* 16 (2006), 2773–2780
- 2 C. Kim, I. Kwon, C. Park, Y. Hwang, H. Bae, B. Yu, C. Pyun, G. Hong, *Journal of Alloys and Compounds* 311 (2000), 33–39
- 3 T. Aitasalo, P. Deren, J. Hölsä, H. Jungner, J.-C. Krupa, M. Lastusaari, J. Legendziewicz, J. Niittykoski and W. Strekc, *Journal of Solid State Chemistry* 171 (2003), 114–122
- 4 Y. Tsunomura, Y. Yoshimine, M. Taguchi, T. Baba, T. Kinoshita, H. Kanno, H. Sakat, E. Maruyama and M. Tanaka, *Solar Energy Materials and Solar Cells* 93 (6–7) (2009), 670–673
- 5 H. Iwai, *Microelectronic Engineering* 86 (2009), 1520–1528
- 6 Y. Pan, M. Wu, Q. Su, *Materials Science and Engineering B* 106 (2004), 251–256
- 7 E. Rasch, *Lighting Design and Application: LD and A*, 7 (9) (1987), 28–34
- 8 J. Emsley, *Nature's Building Blocks, An A-Z Guide to the Element* (2001)
- 9 B. E. Douglas, *Journal of Chemical Education* 31 (11) (1954), 598–599
- 10 G. Hevesy, *Chemical Reviews* 2 (1) (1925), 1–41
- 11 S. Amer, *Revista de Metalurgia* 17 (6) (1981), 377–395.
- 12 J.M. Begovich, W.G. Sisson, *Hydrometallurgy* 10 (1) (1983), 11–20.
- 13 S.N. Flengas, J.E. Dutrizac, *Metallurgical Transactions B* 8B (3) (1977), 377–385
- 14 L. Kumari, G.H. Du, W.Z. Li, R.S. Vennila, S.K. Saxena, D.Z. Wang, *Ceramics International* 35 (2009), 2401–2408
- 15 C. Lu, J.M. Raitano, S. Khalid, L. Zhang and S. Chan, *Journal of Applied Physics* 103 (2008), 124303
- 16 G. Baldinozzi, D. Simeone, D. Gosset and M. Dutheil, *Physical Review Letters* 90 (2003), 216103–1
- 17 R. Terki, G. Bertrand, H. Aourag, C. Coddet, *Materials Letters* 62 (2008), 1484–1486
- 18 H.G. Scott, *Journal of Materials Science* 10 (1975), 1527–1535
- 19 M. Kirm, J. Aarik, M. Jürgens and I. Sildos, *Nuclear Instruments and Methods in Physics Research A* 537 (2005), 251–255
- 20 L.K. Dash, N. Vast, P. Baranek, M. Cheynet and L. Reining, *Physical Review B* 70 (2004), 245116
- 21 A. Emeline, G.V. Kataeva, A.S. Litke, A.V. Rudakova, V.K. Ryabchuk and N. Serpone, *Langmuir* 14 (1998), 5011–5022
- 22 S. Zhao, F. Ma, K.W. Xu, H.F. Liang, *Journal of Alloys and Compounds* 453 (2008), 453–457
- 23 D. Ciuparu, A. Ensuque, G. Shafeev, F. Bozon-Venduras, *Journal of Materials Science Letters* 19 (2000), 931–933
- 24 J. Aarik, H. Mändar, M. Kirm and L. Pung, *Thin Solid Films* 466 (2004), 41–47
- 25 Y.B. Zheng, S.J. Wang, C.H.A. Huan, *Thin Solid Films* 504 (2006), 197–200
- 26 M. Kirm, J. Aarik, M. Jürgens and I. Sildos, *Nuclear Instruments and Methods in Physics Research A* 537 (2005), 251–255
- 27 K. Smits, L. Grigorjeva, W. Łojkowski and J. D. Fidelus, *phys. stat. sol. c* 4 (3) (2007), 770–773
- 28 K. Shunkeev, E. Sarmukhanov, A. Barmina, L. Myasnikova, S. Sagimbaeva and S. Shunkeev, *Physics of the Solid State* 50 (10) (2008), 1799–1802

- 29 K. Smits, D. Millers, L. Grigorjeva, J.D. Fidelus, W. Lojkowski, *Journal of Physics: Conference Series* 93 (2007), 012035
- 30 A. Ciapponi, F. R. Wagner, S. Palmier, J.Y. Natoli, L. Gallais, *Journal of Luminescence* 129 (2009), 1786–1789
- 31 J.E. Geusic, H.M. Marcos and L.G. Van Uitert, *Applied Physics Letters* 4 (10) (1964), 182–184
- 32 I.M. Nagpure, K.N. Shinde, V. Kumara, O.M. Ntwaeaborw, S.J. Dhoble and H.C. Swart, *Journal of Alloys and Compounds* (2009), in press
- 33 L.A. Rocha, E.F. Molina, K.J. Ciuffi, P.S. Calefi and E.J. Nassar, *Materials Chemistry and Physics* 101 (2007), 238–241
- 34 W. Szuszkiewicz, B. Keller, M. Guzik, T. Aitasalo, J. Niittykoski, J. Hölsä, J. Legendziewicz, *Journal of Alloys and Compounds* 341 (2002), 297–306
- 35 E. De la Rosa-Cruz, L.A. Diaz-Torres, P. Salas, R.A. Rodriguez and C. Angeles, *Proc. Of SPIE* 5510 (2004), 57–67
- 36 M. J. Weber, *Physical Review Letters* 171, 283–291
- 37 Z. Assefa, R.G. Haire, P.E. Raison, *Spectrochimica Acta A* 60 (2004), 89–95
- 38 M. Mattarelli, M. Montagna, F. Rossi, C. Tosello, N.D. Afify, M. Bettinelli and A. Speghini, *Optical Materials* 31 (2009), 1362–1365
- 39 T. M. Kozhan, V. V. Kusnetsova, P. R. Pershukovich, I. I. Serqeev, V. S. Khomenko, *Spectrochimica Acta A* 55 (1999), 1407–1409
- 40 H.U. Gudel, M. Pollnau, *Journal of Alloys and Compounds* 303–304 (2000), 307–315
- 41 M. Inokuti and F. Hirajama, *Journal of Chemical Physics* 43 (6) (1965), 1978
- 42 R. Chen, *Journal of Luminescence* 102–103 (2003), 510–518
- 43 A. Ghosh, A.K. Suri, M. Pandey, S. Thomas, T.R. Rama Mohan and B.T. Rao, *Materials Letters* 60 (2006), 1170–1173
- 44 S.A. Tsipas, *Journal of the European Ceramic Society* 30 (2010), 61–72
- 45 R.C. Garvine, M.V. Swain, *Journal of Material Science* 20 (1985), 1193–1200
- 46 W. Qin, C. Nam, H.L. Li, J.A. Szpunar, *Acta Materialia* 55 (2007), 1695–1701
- 47 Y. Zhang, S. Jin, C. Liao, C.H. Yan, *Materials Letters* 56 (2002), 1030–1034
- 48 M. Yoshimur, S. Somiy, *Materials Chemistry and Physics* 61 (1999), 1–8
- 49 M. Mann and J. Kolis, *Journal of Crystal Growth* 312 (2010), 461–465
- 50 D. Tsoutsou, G. Apostolopoulos, S. Galata, P. Tsipas, A. Sotiropoulos, G. Mavrou, Y. Panayiotatos and A. Dimoulas, *Microelectronic Engineering* 86 (2009), 1626–1628
- 51 T. Suntola, J. Antson, U.S. Patent #4058430 (1977)
- 52 J. Aarik, *Disertationes Physicae Universitatis Tartuensis* 49 (2007)
- 53 J. Aarik, A. Aidla, H. Mändar and T. Uustare, *Applied Surface Science* 172 (2001), 148–158
- 54 J. Aarik, A. Aidla, T. Uustare, K. Kukli, V. Sammelselg, M. Ritala and M. Leskelä, *Applied Surface Science* 193 (2002), 277–286
- 55 J. Aarik, A. Aidla, A.-A. Kiisler, T. Uustare and V. Sammelselg, *Thin Solid Films* 340 (1999), 110
- 56 D. Chen, *Solar Energy Materials & Solar Cells* 68 (2001), 313–336
- 57 P.C.A. Jeronimo, A.N. Araujo, M. Conceicao and B. S. M. Montenegro, *Talanta* 72 (2007), 13–27
- 58 T. Tätte, *Disertationes Physicae Universitatis Tartuensis* 59 (2006)
- 59 A. Bisson, A. Rigacci, D. Lecomte, P. Achard, *Journal of Non-Crystalline Solids* 350 (2004), 379–384

- 60 M. Carotta, M. Ferroni, S. Gherardi, V. Guidi, C. Malagu, G. Martinelli, M. Sacerdoti, M. Di Vona, S. Licoccia and E. Traversa, *Journal of the European Ceramic Society* 24 (2004), 1409–1413
- 61 V. Reedo, M. Järvekülg, A. Lõhmus and U. Mäeorg, *Physica Status Solidi A* 205 (6) (2008), 1511–1514
- 62 H. R. Harrison and J. M. Honig, *Bulletin of Material Science* 3 (3) (1981), 247–253
- 63 J. Xu, X. Lei, X. Jiang, Q. He, Y. Fang, D. Zhang and X. He, *Journal of Rare Earths* 27 (6) (2009), 971–974
- 64 M. Hartmanova, F. Kubel, V. Burkova, M. Jergel, V. Navrátil, E.E. Lomonova, K. Navratil, F. Kundracik and I. Kosti, *Russian Journal of Electrochemistry* 43 (4) (2007), 381–389
- 65 D.J. Buttrey, H.R. Harrison, J.M. Honig and R.R. Schartman, *Journal of Solid State Chemistry* 54 (3) (1984), 407–413
- 66 N. E. W. Hartley, *Tribology International* 8 (2) (1975), 65–72
- 67 V. V. Yudin, *Applied Physics* 15 (1978), 223–228
- 68 K. Pearson, *Proceedings of the Royal Society of London* 54 (1893), 329–333.
- 69 J.P. Biersack and L.G. Haggmark, *Nuclear Instruments and Methods B* 174 (1980), 257.
- 70 <http://www.srim.org/>
- 71 J. Aarik, A. Aidla, H. Mändar and T. Uustare, *Applied Surface Science* 172 (2001), 148–158
- 72 <http://accelrys.com/products/materials-studio/index.html>
- 73 M.D. Segall, P.J.D. Lindan, M.J. Probert, C.J. Pickard, P.J. Hasnip, S.J. Clark and M.C. Payne, *Journal of Physics: Condensed Matter* 14 (2002), 2717
- 74 D.M. Ramo, P.V. Sushko, J.L. Gavartin and A.L. Shluger, *Physical Review B* 78 (2008), 235432
- 75 D.M. Ramo and A.L. Shluger, *Journal of Physics: Conference Series* 117 (2008) , 012022
- 76 C. Morant, A. Fernandez, A. R. Gonzalez-Elipé, L. Soriano, A. Stampfl, A. M. Bradshaw and A. M. Sanz, *Physical Review B* 52 (1995). 11711
- 77 S. Du, J. Xu, X. Dong, J. Zhang, Z. Fu and Z. Dai, *Journal of Luminescence* (2010), article in press
- 78 M.J. Treadaway and R.C. Powell, *Physical Review B* 11 (2) (1975), 862–874
- 79 N. Dong, M. Yin, L. Ning, H. Guo and W. Zhang, *Journal of Alloys and Compounds* 424 (2006), 334
- 80 R.T. Wegh, E.V.D. van Loef and A. Meijerink, *Journal of Luminescence* 90 (2000), 111–122
- 81 U.V. Kumar, D.R. Rao and P. Venkateswarlu, *Journal of chemical Physics* 66 (5) (1977)
- 82 P. Dorenbos, *Journal of Physics: Condensed Matter* 15 (2003), 8417–8434
- 83 P. Dorenbos, *Journal of Luminescence* 108 (2004), 301–305
- 84 P. Dorenbos, *Journal of Luminescence* 111 (2005), 89–104
- 85 P. Dorenbos, *Journal of Alloys and Compounds* 488 (2009), 568–573
- 86 H. Liu, L. Wang, S. Chen and B. Zou, *Journal of Alloys and Compounds* 448 (2008), 336–339
- 87 L. Laversenne, C. Goutaudier, Y. Guyot, M. Th. Cohen-Adad, G. Boulon, *Journal of Alloys and Compounds* 341 (2002), 214–219

- 88 H. Elhouichet, S. Daboussi, H. Ajlani, A. Najar, A. Moadhen, M. Oueslati, I. M. Tiginyanu, S. Langa and H. Föll, *Journal of Luminescence* 113 (2005), 329–337
- 89 A.D. Sontakke, K. Biswas, K. Annapurna, *Journal of Luminescence* 129 (2009), 1347–1355
- 90 R.H.R. Castro, P.J.B. Marcos, A. Lorriaux, M.C. Steil, L. Gengembre, P. Roussel and D. Gouvea, *Chemical Materials* 20 (2008), 3505–3511
- 91 D. Gazzoli, G. Mattei and M. Valigi and J. Raman Spectroscopy 38 (2007), 824–831
- 92 S. Mahlik, M. Zalewska, M. Grinberg, A. M. Konkowski and M. Godlewski, *Journal of Luminescence* 128 (2008), 921–923
- 93 J. Trojan-Piegza, E. Zych, J. Hölsä and J. Niittykoski, *Journal of Physical Chemistry C* 113 (2009), 20493–20498
- 94 V. Venkatramu, P. Babu, C.K. Jayasankar, T. Tröster, W. Sievers, G. Wortmann, *Optical Materials* 29 (2007), 1429–1439
- 95 M. Yamaga, Y. Masui, S. Sakuta, N. Kodama, K. Kaminaga, *Physical Review B* 71 (2005), 205102
- 96 U. Ranon, *Journal of Physics and Chemistry of Solids* 25 (11) (1964), 1205–1212
- 97 D. Megías, R. Marrero, B. Martínez, M. García, J. Bravo-Cordero, A. García-Grande, A. Santos and M. Montoya, *Microscopy Research and Technique* 72 (2009), 1–11
- 98 B. Kim and H. Hamaguchi, *Physica Status Solidi B* 203 (1997), 557
- 99 D.R. Clarke and F. Adar, *Journal of American Ceramic Society* 65 (1982), 284
- 100 V. Kiisk, I. Sildos, S. Lange, V. Reedo, T. Tätte, M. Kirm and J. Aarik, *Applied Surface Science* 247 (2005), 412–417
- 101 E. De la Rosa-Cruz, L.A. Diaz-Torres, P. Salas, R. A. Rodriguez, G. A. Kumar, M. A. Meneses, J. F. Mosin, J. M. Hernandez and O. Barbosa-Garcia, *Journal of Applied Physics* 94 (5) (2003), 3509–3515
- 102 Y.P. Udalov, D.V. Grishchenko, V.V. Kulakov, I.V. Poznyak and A.Y. Pechenkov, *Glass Physics and Chemistry* 34 (5) (2008), 623–633
- 103 A.V. Emeline, N. Serpone, *Chemical Physics Letter* 345 (2001), 105–110
- 104 W. Qin, C. Nam, H.L. Li and J.A. Szpunar, *Acta Materialia* 55 (2007), 1695–1701



## ACKNOWLEDGEMENTS

First and foremost the author of the dissertation would like to thank his supervisor Ilmo Sildos for persistent and constructive support in understanding, conducting and presenting the various aspects of the work. His ideological guidance has been the driving force for conducting many of the experimental work as well as selecting the studied materials.

Additionally author wants to thank his co-worker Valter Kiisk for his long-term experimental and theoretical guidance. Mikhail Brik is acknowledged for the theoretical discussions and calculations related to developing the understanding of the electronic band structure of the studied materials.

Help at the different experimental facilities used during the work was kindly provided by: Martti Pärs, Mihkel Rähn, Ahti Niilisk, Hugo Mändar, Eduard Feldbach, Marco Kirm, Vitali Nagirnõi, Vambola Kisand, Ilmar Kink and Aleksei Kotlov.

The experimental samples studied were prepared by Jaan Aarik, Tanel Tätte, Valter Reedo, Martin Järvekülg, Kathriin Utt, Elena Lomonova. The financial support from Estonian Science Fund grants 5864, 5861, 6999, 6658, 6660 has been used during several stages of the work. Additionally the support has been received from TÜ and TTÜ doctoral schools: Funktsionaalsete materjalide ja tehnoloogiate doktorikool” (FMTDK) and “Materjaliteaduse ja materjalide tehnoloogia doktorikool” (MMDTK). The experiments at Hasylab synchrotron radiation laboratory were financed by European Community's 6th and 7th Framework Programme under grant agreements n° RII-CT-2004-506008 and 226716. Ion-implantation experiments in Uppsala (Sweden) were supported by Framework Six “Access to Research Infrastructure” action of the “Improving Human Potential Programme”.



## **PUBLICATIONS**

# CURRICULUM VITAE (CV)

## Sven Lange

### General data

Date and place of birth	14. June 1980, Tallinn
Citizenship	Estonian
Marital Status	unmarried partners
Children	Rasmus Lange (23.07.2009)
Contact	Institute of Physics, University of Tartu Riia 142 St, 51014 Tartu
Tel	+3725541860
E-mail	lange.sven@gmail.com

### Education

2005–2010	Tartu University, PhD student (solid state physics)
2003–2005	Tartu University, MSc (material science)
1999–2003	Tartu University, BSc (physics)
1996–1999	Hugo Treffner Gymnasium
1990–1996	Tartu 12. High school
1987–1990	Tallinn 4. High school

### Language skills

Estonian	mother tongue
English	good in speaking and writing
Finnish	average speaking, basic writing
Russian	basic
German	basic

### Professional employment

06.2008 – ...	AS Estiko Plastar, scientific project manager
09.2003–06.2008	OÜ Playtech Estonia, corporate client manager
09.2002 – ...	Tartu Physics Institute, laboratory assistant

### Supervised dissertations

2009	Kathriin Utt, BA (co-supervised) “Erineva struktureerituse astmega metalloksiidmaterjalide valmistamine ja optiline karakteriseerimine”
2006	Mari Shavel, BSc. “Tehisteemandi ja rubiini kristallide kasutamine optiliste temperatuurianduritena”
2005	Marti Tamm, BSc. “Eu <sup>3+</sup> ja Er <sup>3+</sup> ioonidega dopeeritud TiO <sub>2</sub> kilematerjalide luminesentsuuringud.”

## Awards

- 2005 Student stipend of the Institute of Physics University of Tartu  
2003 Student stipend of the Institute of Physics University of Tartu

## List of publications

- K. Utt, S. Lange, M. Järvekülg, H. Mändar, P. Kanarjov, I. Sildos, "*Structure and optical properties of Sm-doped ZrO<sub>2</sub> microrolls*", Optical Materials (2010), In Press
- S. Lange, I. Sildos, M. Hartmanova, V. Kiisk, E. E. Lomonova and M. Kirm, "*Optical Investigation of Sm doped ZrO<sub>2</sub>*", Journal of Physics: Conference Series (2010), Accepted for publication
- V. Kiisk, S. Lange, K. Utt, T. Tätte, H. Mändar and I. Sildos, "*Photoluminescence of sol-gel-prepared hafnia*", Physica B: Condensed Matter 405 (2) (2010), 758–762
- S. Lange, I. Sildos, M. Hartmanova, J. Aarik and V. Kiisk, "*Luminescence properties of Sm<sup>3+</sup>-doped polycrystalline ZrO<sub>2</sub>*", Journal of Non-Crystalline Solids 354 (2008), 4380–4382
- S. Lange, V. Kiisk, J. Aarik, M. Kirm and I. Sildos, "*Luminescence of ZrO<sub>2</sub> and HfO<sub>2</sub> thin films implanted with Eu and Er ions*", Physica Status Solidi (c) 3 (2007), 938–941
- S. Lange, V. Kiisk, V. Reedo, M. Kirm, J. Aarik and I. Sildos, "*Luminescence of RE-ions in HfO<sub>2</sub> thin films and some possible applications.*", Optical Materials 28 (2006), 1238–1242
- S. Lange, I. Sildos, V. Kiisk, M. Kirm, "*Photoluminescence of RE-doped thin metal-oxide films*", Physica Status Solidi (c) 2 (1) (2005), 326–329
- V. Reedo, S. Lange, V. Kiisk, A. Lukner, T. Tätte and I. Sildos, "*Influence of ambient gas on the photoluminescence of sol-gel derived TiO<sub>2</sub>:Sm<sup>3+</sup> films*", Optical Materials and Applications, Proceedings of SPIE 5946 (2005), 59460F1–6
- V. Kiisk, I. Sildos, S. Lange, V. Reedo, T. Tätte, M. Kirm and J. Aarik, "*Photoluminescence characterization of pure and Sm<sup>3+</sup>-doped thin metaloxide films*", Applied Surface Science 247 (2005), 412–417
- J. Aarik, A. Kasikov, M. Kirm, S. Lange, T. Uustare and H. Mändar, "*Optical properties of crystalline Al<sub>2</sub>O<sub>3</sub> thin films grown by atomic layer deposition*", Proc. of SPIE 5946 (2005), 594601
- S. Lange, I. Sildos, V. Kiisk and J. Aarik, "*Energy transfer in the photoexcitation of Sm<sup>3+</sup> implanted TiO<sub>2</sub> thin films*", Materials Science and Engineering B 112 (2004), 87–90
- I. Sildos, S. Lange, T. Tätte, V. Kiisk, M. Kirm and J. Aarik, "*Emission of rare earth ions incorporated into metal oxide thin films and fibres*", Mat. Res. Soc. Symp. Proc. 796 (2004), 361–366
- I. Sildos, V. Kiisk, S. Lange and J. Aarik, "*Time-resolved exciton-emission spectroscopy of anatase*", Proceedings of SPIE 5122 (2003), 56–59

## Other activities

Member of the "Physics Program Board" of University of Tartu (since 2009).

# ELULOO KIRJELDUS (CV)

## Sven Lange

### Üldandmed

Sünni aeg ja koht	14. juuni 1980, Tallinn
Kodakondsus	Estonian
Perekonnaseis	Vabaabielus
Lapsed	Rasmus Lange (23.07.2009)
Kontakt	Füüsika Instituut, Tartu Ülikool Riia 142, 51014 Tartu
Tel.	+3725541860
E-mail	lange.sven@gmail.com

### Haridustee

2005–2010	Tartu Ülikool, doktorant (tahkisefüüsika)
2003–2005	Tartu Ülikool, MSc (materjaliteadus)
1999–2003	Tartu Ülikool, BSc (füüsika)
1996–1999	Hugo Treffner Gümnaasium
1990–1996	Tartu 12. keskkool
1987–1990	Tallinn 4. keskkool

### Keeleoskus

eesti	emakeel
inglise	hea kõnes ja kirjas
soome	keskmise kõnes, algeline kirjas
vene	algeline
Saksa	algeline

### Töökogemus

06.2008 – ...	AS Estiko Plastar, teadusprojektide projektijuht
09.2003–06.2008	OÜ Playtech Estonia, korporatiivkliendi haldur
09.2002 – ...	Tartu Ülikooli Füüsika Instituut, assistent

### Juhendatud dissertatsioonid

2009	Kathriin Utt, BA (kaasjuhendamine) “Erineva struktureerituse ast-mega metalloksiidmaterjalide valmistamine ja optiline karakteri-seerimine”
2006	Mari Shavel, BSc. “Tehisteemandi ja rubiini kristallide kasutamine optiliste temperatuurianduritena”
2005	Martti Tamm, BSc. “Eu <sup>3+</sup> ja Er <sup>3+</sup> ionidega dopeeritud TiO <sub>2</sub> kile-materjalide luminesentsuuringud.”

## Auhinnad

- 2005 Tartu Ülikooli Füüsika Instituudi üliõpilasstipendium (ühekordne)  
2003 Tartu Ülikooli Füüsika Instituudi üliõpilasstipendium (ühekordne)

## Publikatsioonid

- K. Utt, S. Lange, M. Järvekülg, H. Mändar, P. Kanarjov, I. Sildos, "*Structure and optical properties of Sm-doped ZrO<sub>2</sub> microrolls*", Optical Materials (2010), In Press
- S. Lange, I. Sildos, M. Hartmanova, V. Kiisk, E. E. Lomonova and M. Kirm, "*Optical Investigation of Sm doped ZrO<sub>2</sub>*", Journal of Physics: Conference Series (2010), Accepted for publication
- V. Kiisk, S. Lange, K. Utt, T. Tätte, H. Mändar and I. Sildos, "*Photoluminescence of sol-gel-prepared hafnia*", Physica B: Condensed Matter 405 (2) (2010), 758–762
- S. Lange, I. Sildos, M. Hartmanova, J. Aarik and V. Kiisk, "*Luminescence properties of Sm<sup>3+</sup>-doped polycrystalline ZrO<sub>2</sub>*", Journal of Non-Crystalline Solids 354 (2008), 4380–4382
- S. Lange, V. Kiisk, J. Aarik, M. Kirm and I. Sildos, "*Luminescence of ZrO<sub>2</sub> and HfO<sub>2</sub> thin films implanted with Eu and Er ions*", Physica Status Solidi (c) 3 (2007), 938–941
- S. Lange, V. Kiisk, V. Reedo, M. Kirm, J. Aarik and I. Sildos, "*Luminescence of RE-ions in HfO<sub>2</sub> thin films and some possible applications.*", Optical Materials 28 (2006), 1238–1242
- S. Lange, I. Sildos, V. Kiisk, M. Kirm, "*Photoluminescence of RE-doped thin metal-oxide films*", Physica Status Solidi (c) 2 (1) (2005), 326–329
- V. Reedo, S. Lange, V. Kiisk, A. Lukner, T. Tätte and I. Sildos, "*Influence of ambient gas on the photoluminescence of sol-gel derived TiO<sub>2</sub>:Sm<sup>3+</sup> films*", Optical Materials and Applications, Proceedings of SPIE 5946 (2005), 59460F1–6
- V. Kiisk, I. Sildos, S. Lange, V. Reedo, T. Tätte, M. Kirm and J. Aarik, "*Photoluminescence characterization of pure and Sm<sup>3+</sup>-doped thin metaloxide films*", Applied Surface Science 247 (2005), 412–417
- J. Aarik, A. Kasikov, M. Kirm, S. Lange, T. Uustare and H. Mändar, "*Optical properties of crystalline Al<sub>2</sub>O<sub>3</sub> thin films grown by atomic layer deposition*", Proc. of SPIE 5946 (2005), 594601
- S. Lange, I. Sildos, V. Kiisk and J. Aarik, "*Energy transfer in the photoexcitation of Sm<sup>3+</sup> implanted TiO<sub>2</sub> thin films*", Materials Science and Engineering B 112 (2004), 87–90
- I. Sildos, S. Lange, T. Tätte, V. Kiisk, M. Kirm and J. Aarik, "*Emission of rare earth ions incorporated into metal oxide thin films and fibres*", Mat. Res. Soc. Symp. Proc. 796 (2004), 361–366
- I. Sildos, V. Kiisk, S. Lange and J. Aarik, "*Time-resolved exciton-emission spectroscopy of anatase*", Proceedings of SPIE 5122 (2003), 56–59

## Muud tegevus

Tartu Ülikooli füüsika programminõukogu liige alates 2009 aastats.

## DISSERTATIONES PHYSICAE UNIVERSITATIS TARTUENSIS

1. **Andrus Ausmees.** XUV-induced electron emission and electron-phonon interaction in alkali halides. Tartu, 1991.
2. **Heiki Sõnajalg.** Shaping and recalling of light pulses by optical elements based on spectral hole burning. Tartu, 1991.
3. **Sergei Savihhin.** Ultrafast dynamics of F-centers and bound excitons from picosecond spectroscopy data. Tartu, 1991.
4. **Ergo Nõmmiste.** Leelishalogeniidide röntgenelektronemissioon kiirita-misel footonitega energiaga 70–140 eV. Tartu, 1991.
5. **Margus Rätsep.** Spectral gratings and their relaxation in some low-tempe-rature impurity-doped glasses and chrystals. Tartu, 1991.
6. **Tõnu Pullerits.** Primary energy transfer in photosynthesis. Model calcula-tions. Tartu, 1991.
7. **Olev Saks.** Attoampri diapasoonis voolude mõõtmise füüsikalised alused. Tartu, 1991.
8. **Andres Virro.** AlGaAsSb/GaSb heterostructure injection lasers. Tartu, 1991.
9. **Hans Korge.** Investigation of negative point discharge in pure nitrogen at atmospheric pressure. Tartu, 1992.
10. **Jüri Maksimov.** Nonlinear generation of laser VUV radiation for high-reso-lution spectroscopy. Tartu, 1992.
11. **Mark Aizengendler.** Photostimulated transformation of aggregate defects and spectral hole burning in a neutron-irradiated sapphire. Tartu, 1992.
12. **Hele Siimon.** Atomic layer molecular beam epitaxy of  $A^2B^6$  compounds described on the basis of kinetic equations model. Tartu, 1992.
13. **Tõnu Reinot.** The kinetics of polariton luminescence, energy transfer and relaxation in anthracene. Tartu, 1992.
14. **Toomas Rõõm.** Paramagnetic  $H^{2-}$  and  $F^+$  centers in CaO crystals: spectra, relaxation and recombination luminescence. Tallinn, 1993.
15. **Erko Jalviste.** Laser spectroscopy of some jet-cooled organic molecules. Tartu, 1993.
16. **Alvo Aabloo.** Studies of crystalline celluloses using potential energy calcu-lations. Tartu, 1994.
17. **Peeter Paris.** Initiation of corona pulses. Tartu, 1994.
18. **Павел Рубин.** Локальные дефектные состояния в  $CuO_2$  плоскостях высокотемпературных сверхпроводников. Тарту, 1994.
19. **Olavi Ollikainen.** Applications of persistent spectral hole burning in ultra-fast optical neural networks, time-resolved spectroscopy and holographic interferometry. Tartu, 1996.
20. **Ülo Mets.** Methodological aspects of fluorescence correlation spectroscopy. Tartu, 1996.
21. **Mikhail Danilkin.** Interaction of intrinsic and impurity defects in CaS:Eu luminophors. Tartu, 1997.



22. **Ирина Кудрявцева.** Создание и стабилизация дефектов в кристаллах KBr, KCl, RbCl при облучении ВУФ-радиацией. Тарту, 1997.
23. **Andres Osvet.** Photochromic properties of radiation-induced defects in diamond. Tartu, 1998.
24. **Jüri Örd.** Classical and quantum aspects of geodesic multiplication. Tartu, 1998.
25. **Priit Sarv.** High resolution solid-state NMR studies of zeolites. Tartu, 1998.
26. **Сергей Долгов.** Электронные возбуждения и дефектообразование в некоторых оксидах металлов. Тарту, 1998.
27. **Kaupo Kukli.** Atomic layer deposition of artificially structured dielectric materials. Tartu, 1999.
28. **Ivo Heinmaa.** Nuclear resonance studies of local structure in  $\text{RBa}_2\text{Cu}_3\text{O}_{6+x}$  compounds. Tartu, 1999.
29. **Aleksander Shelkan.** Hole states in  $\text{CuO}_2$  planes of high temperature superconducting materials. Tartu, 1999.
30. **Dmitri Nevedrov.** Nonlinear effects in quantum lattices. Tartu, 1999.
31. **Rein Ruus.** Collapse of 3d (4f) orbitals in 2p (3d) excited configurations and its effect on the x-ray and electron spectra. Tartu, 1999.
32. **Valter Zazubovich.** Local relaxation in incommensurate and glassy solids studied by Spectral Hole Burning. Tartu, 1999.
33. **Indrek Reimand.** Picosecond dynamics of optical excitations in GaAs and other excitonic systems. Tartu, 2000.
34. **Vladimir Babin.** Spectroscopy of exciton states in some halide macro- and nanocrystals. Tartu, 2001.
35. **Toomas Plank.** Positive corona at combined DC and AC voltage. Tartu, 2001.
36. **Kristjan Leiger.** Pressure-induced effects in inhomogeneous spectra of doped solids. Tartu, 2002.
37. **Helle Kaasik.** Nonperturbative theory of multiphonon vibrational relaxation and nonradiative transitions. Tartu, 2002.
38. **Tõnu Laas.** Propagation of waves in curved spacetimes. Tartu, 2002.
39. **Rünno Lõhmus.** Application of novel hybrid methods in SPM studies of nanostructural materials. Tartu, 2002.
40. **Kaido Reivelt.** Optical implementation of propagation-invariant pulsed free-space wave fields. Tartu, 2003.
41. **Heiki Kasemägi.** The effect of nanoparticle additives on lithium-ion mobility in a polymer electrolyte. Tartu, 2003.
42. **Villu Repän.** Low current mode of negative corona. Tartu, 2004.
43. **Алексей Котлов.** Оксианионные диэлектрические кристаллы: зонная структура и электронные возбуждения. Тарту, 2004.
44. **Jaak Talts.** Continuous non-invasive blood pressure measurement: comparative and methodological studies of the differential servo-oscillometric method. Tartu, 2004.
45. **Margus Saal.** Studies of pre-big bang and braneworld cosmology. Tartu, 2004.

46. **Eduard Gerškevitš.** Dose to bone marrow and leukaemia risk in external beam radiotherapy of prostate cancer. Tartu, 2005.
47. **Sergey Shchemelyov.** Sum-frequency generation and multiphoton ionization in xenon under excitation by conical laser beams. Tartu, 2006.
48. **Valter Kiisk.** Optical investigation of metal-oxide thin films. Tartu, 2006.
49. **Jaan Aarik.** Atomic layer deposition of titanium, zirconium and hafnium dioxides: growth mechanisms and properties of thin films. Tartu, 2007.
50. **Astrid Rekker.** Colored-noise-controlled anomalous transport and phase transitions in complex systems. Tartu, 2007.
51. **Andres Punning.** Electromechanical characterization of ionic polymer-metal composite sensing actuators. Tartu, 2007.
52. **Indrek Jõgi.** Conduction mechanisms in thin atomic layer deposited films containing  $\text{TiO}_2$ . Tartu, 2007.
53. **Aleksei Krasnikov.** Luminescence and defects creation processes in lead tungstate crystals. Tartu, 2007.
54. **Küllike Rägo.** Superconducting properties of  $\text{MgB}_2$  in a scenario with intra- and interband pairing channels. Tartu, 2008.
55. **Els Heinsalu.** Normal and anomalously slow diffusion under external fields. Tartu, 2008.
56. **Kuno Kooser.** Soft x-ray induced radiative and nonradiative core-hole decay processes in thin films and solids. Tartu, 2008.
57. **Vadim Boltrushko.** Theory of vibronic transitions with strong nonlinear vibronic interaction in solids. Tartu, 2008.
58. **Andi Hektor.** Neutrino Physics beyond the Standard Model. Tartu, 2008.
59. **Raavo Josepson.** Photoinduced field-assisted electron emission into gases. Tartu, 2008.
60. **Martti Pärs.** Study of spontaneous and photoinduced processes in molecular solids using high-resolution optical spectroscopy. Tartu, 2008.
61. **Kristjan Kannike.** Implications of neutrino masses. Tartu, 2008.
62. **Vigen Issahhanjan.** Hole and interstitial centres in radiation-resistant  $\text{MgO}$  single crystals. Tartu, 2008.
63. **Veera Krasnenko.** Computational modeling of fluorescent proteins. Tartu, 2008.
64. **Mait Müntel.** Detection of doubly charged higgs boson in the CMS detector. Tartu, 2008.
65. **Kalle Kepler.** Optimisation of patient doses and image quality in diagnostic radiology. Tartu, 2009.
66. **Jüri Raud.** Study of negative glow and positive column regions of capillary HF discharge. Tartu, 2009.